A fine-resolution soil moisture dataset for China in 2002-2018

Xiangjin Meng[1,2,★], Kebiao Mao[3,★], Fei Meng[4], Jiancheng Shi[5,6], Jiangyuan Zeng[6], Xinyi Shen[7], Yaokui Cui[8], Lingmei Jiang[6], and Zhonghua Guo[1]

[1] School of Physics and Electronic-Engineering, Ningxia University, Yinchuan 750021, China.
[2] School of Earth Sciences and Engineering, Hohai University, Nanjing 211100, China.
[3] Institute of Agricultural Resources and Regional Planning, Chinese Academy of Agricultural Sciences, Beijing, 100081, China
[4] School of Surveying and Geo-Informatics, Shandong Jianzhu University, Jinan, 250100, China.
[5] National Space Science Center, Chinese Academy of Sciences, Beijing, 100190, China.
[6] State Key Laboratory of Remote Sensing Science, Jointly Sponsored by the Aerospace Information Research Institute of Chinese Academy of Sciences and Beijing Normal University, Beijing, 100101, China.
[7] Civil and Environmental Engineering, University of Connecticut, Storrs, CT 06269, USA.
[8] School of Earth and Space Sciences, Peking University, Beijing, China, 100871.

Correspondence to: Kebiao Mao (maokebiao@caas.cn)

★ These authors contributed equally to this work.

Abstract: Soil moisture is an important parameter required for agricultural drought monitoring and climate change models. Passive microwave remote sensing technology has become an important means to quickly obtain soil moisture ~~over~~ across large areas, but the coarse spatial resolution of microwave data imposes great limitations on the application of these data. We provide a unique soil moisture dataset (0.05°, monthly) for China from 2002-2018 based on reconstruction model-based downscaling techniques using soil moisture data from different passive microwave products (including ~~the~~ AMSR-E/2 JAXA Level 3 products and ~~the~~ SMOS-INRA-CESBIO (SMOS-IC) products) calibrated with a consistent model in combination with ground observation data. This new fine-resolution soil moisture dataset with a high spatial resolution overcomes the multisource data time matching problem between optical and microwave data sources and eliminates the difference between the different sensor observation errors. The validation analysis indicates that the accuracy of the new dataset is satisfactory (bias: ~~-0.024, -0.030 and -0.016~~ -0.057, −0.063 to -0.027 $m^3/m^3$$m^3/m^3$, unbiased root mean square error (*ub*RMSE): ~~0.051, 0.048 and 0.042~~0.056, 0.036 and 0.048, correlation coefficient (*R*): ~~0.82, 0.88, and 0.90~~ 0.84, 0.85, and 0.89 on monthly, seasonal and annual scales, respectively). The new dataset was used to analyze the spatiotemporal patterns of soil water content across China from 2002 to 2018. In the past 17 years, China's soil moisture has shown cyclical fluctuations and a slight downward trend ~~(slope=-0.167, *R*=0.750)~~ and can be summarized as wet in the south and dry in the north, with increases in the west and decreases in the east. The reconstructed dataset can be widely used to significantly improve hydrologic and drought monitoring and can serve as an important input for ecological and other geophysical models. The data are published in ~~the~~ Zenodo at http:~~//doi.org/10.5281/zenodo.4049958 (Meng et al., 2020)~~ //doi.org/10.5281/zenodo.4738556 (Meng et al 2021).

Keywords: Downscaling, Soil moisture, Passive microwave, Spatial weighted decomposition (SWD) model, China, TVDI

1 Introduction

Soil moisture (SM), which is one of the key variables in ~~the~~ water cycle and atmospheric energy budget (Entekhabi et al., 1999; Taylor et al., 2011; Shi et al., 2012; Guillod et al., 2015), has been widely used for flood forecasts (Bindlish, et al., 2009), drought detection (Mao, et al., 2010), crop yield estimation (Chen, et al., 2011), weather prediction and hydrological modeling (Liu, et al., 2017). Therefore, accurately monitoring and assessing the dynamics of the spatiotemporal distribution of SM are crucial for understanding the hydrological, ecological, and biogeochemical processes associated with global and regional climate systems (Mao et al., 2008b; Seneviratne et al., 2010; Han et al., 2012; Wang et al., 2016). The most direct way to obtain SM is primarily from in situ measurements with SM measuring instruments at ground meteorological stations (Franz et al., 2012). SM networks based on ground stations have made great contributions to establishing long-term SM datasets (Srivastava 2016). The in situ SM observations from these networks have also been unified into a common database (Dorigo et al., 2011). However, ~~the~~ accurate measurements of SM are limited by the number of field sites around the world, and measuring SM at a single location does not necessarily represent the condition of ~~the~~ an entire region due to the large spatial heterogeneity of SM (Crow et al., 2002; Njoku et al., 2003). With the development of remote sensing technology, satellite-based SM measurements has become ~~increasingly available, such as microwave observations from active and passive sensors, which is~~ one of the most effective and rapid methods to obtain large-scale SM (Loew, et al., 2011; Petropoulos, et al., 2015; Srivastava, et al., 2017). Microwave remote sensing, including active microwave and passive microwave, has become the most effective means of monitoring SM ~~active microwave remote sensing technology measures the energy reflected from the surface of the land after actively transmitting microwave energy pulses, while passive microwave sensors measure the self-emitted energy emitted from the land surface~~ (Schmugge et al., 1974; Moran, et al., 2004; Shi et al., 2006; Shen et al., 2013; Bhagat et al., 2014), B~~oth active and passive microwave remote instruments, particularly at low frequencies~~, which have been used to provide global coverage for surface ~~soil moisture~~ SM datasets (Njoku, 2003; Albergel, et al., 2013). The European Space Agency's Water Cycle Multi-Mission Observation Strategy (ESA WACMOS) Support to Science Element (STSE) program has developed the first long-term SM data record from passive and active microwave data (Su et al. 2010). In 2012, the ESA's Climate Change Initiative (CCI) program SM datasets were first publicized on the ESA CCI web portal ~~(Su et al., 2010).~~ This CCI product was generated by merging different microwave sensor observations and attempting to produce a complete and consistent long-term time series of SM datasets (Dorigo et al., 2017; Gruber et al. 2019). Since then, it has been constantly updated, and the latest release (v06.1)~~(v05.2)~~ provides global SM data up to 2020-12-31 ~~31-12-2019~~. ~~These~~ The long-term availability of SM products has been validated against extensive model simulations or in situ measurements (Albergel et al., 2012; Loew et al., 2013; Zeng et al., 2015; Dorigo et al., 2017, Preimesberger et al 2021). ~~and~~ Kang et al (2020) improved the algorithm for FY 3D microwave data and also produced a global SM product (Kang et al. 2020), and the resolution is about 0.25-degree resolution covering 2017-2019. Chen et al. (2021) develop a novel spatiotemporal partial convolutional neural network (CNN) for AMSR2 soil moisture product gap-filling, and the resolution is about 0.25-degree resolution covering 2003–2019.

Although the SM datasets mentioned above can provide SM parameters for global climate change research, the resolution is relatively low (e.g., 10 km or 25 km),which is very difficult to meet local refined research, especially agricultural drought menitoring. In order to obtain a soil moisture data set with high spatial resolution, various methods have been proposed to downscale SM. ~~these products are widely used for a range of soil moisture- SM related studies, such as climate model evaluation and drought monitoring. The mentioned SM datasets have a coarse spatial resolution (e.g., 25 km), whereas a high-resolution SM product that can be directly used in hydrological process models (e.g., surface evapotranspiration models, land surface process models, and agricultural drought models) in regional-scale or local-scale studies is needed to provide additional monitoring details, unless a fine-resolution land surface SM product (e.g., from 1 to 10 km) is available. Downscaled SM data can help to solve the problem of coarse spatial resolution and are required for many regional agricultural and hydrological applications~~ (Sandholt et al. 2002, Peng et al. 2015, Mohanty et al. 2017). ~~To improve the spatial resolution of passive microwave SM data, various methods have been proposed to downscale SM. The basic principle of this most approaches is that to construct a statistical correlation or physical model relationship between coarse-resolution SM data and fine-resolution auxiliary variables to achieve scale conversion.~~ The basic principle of most methods is that the drought index constructed using high-resolution visible light and thermal infrared data has a strong linear relationship with microwave soil moisture in local areas (Jin et al. 2017, Maltese et al. 2015, Wang et al. 2016). ~~Some of these studies have tried to explore the relationship between optical remote sensing products with a relatively fine spatial resolution and microwave remote sensing SM data with a coarse spatial resolution (Maltese et al. 2015, Wang et al. 2016). Due to the difference in coverage between vegetation cover and bare soil, the sensitivity of land surface temperature (LST) to SM changes varies, and the shapes of plotted LSTs and normalized difference vegetation index (NDVI) data values are usually presented in a physical sense as in trapezoidal or triangular feature space (Carlson et al. 1994, Moran et al. 1994) if the data can represent the complete vegetation cover and soil water content. Based on the LST/ normalized difference vegetation (NDVI) feature space, the temperature vegetation dryness index (TVDI) has been developed to estimate the SM~~ The temperature vegetation dryness index (TVDI) was developed to estimate the SM (Sandholt 2002), which is the most classic method and has been widely used for the downscaling of microwave SM and drought monitoring over different regions (Chauhan et al. 2003). ~~Meanwhile, the TVDI has been widely used for the downscaling of microwave SM and drought monitoring over different regions (Chauhan et al. 2003). However, a significant problem in the downscaling process is the time matching of different sensors, that is, the temporal gap between the coarse-resolution microwave product and the fine-resolution optical product~~ Jing et al. (2018) proposed a two-steps reconstruction approach for reconstructing satellite-based soil moisture products (ECV) at an improved spatial 0.05-degree resolution covering 2001–2012. The reconstruction model implemented the Random Forests (RF) regression algorithm to simulate the relationships between soil moisture and environmental variables, and takes advantages of the high spatial resolution of optical remote sensing products (Jing et al, 2018). Most downscaling data sets are mainly for a single sensor. Due to the limitation of the lifetime of satellite sensors, the time series is not long enough, and it is difficult to analyze the temporal and spatial changes of a long time series. Different satellite microwave sensors have differences in time and space, and the depth information of SM detected by the different frequencies of different microwave sensors is not consistent. In order to obtain a longer time sequence of SM dataset, we must eliminate the differences between different sensors (Peng et al., 2017). ~~This interval can cause a lager~~ large ~~deviation between~~ the ~~downscaled products and original product, such as differences in daytime and nighttime surface temperatures, humidity, evapotranspiration, water and heat. This~~ problem ~~requires obtaining SM and auxiliary optical/infrared (IR) data with relatively consistent time points. It is generally difficult to aggregated~~ aggregate ~~data from long-sequence multisource sensors while taking into account most of the sensors.~~ Many methods have been proposed to handle these systematic differences among SM products from different microwave sensors (Zwieback, et al., 2016). Recent studies have exploited the utility of rescaling SM product methods (Brocca et al., 2013; Zeng et al., 2020). Linear regression rescaling of SM has proven to be a simple and effective method, and a review of these rescaling methods ~~has been~~ was published by Afshar et al. (2017). In addition, in the process of downscaling, optical and thermal infrared data should be synchronized with microwave soil moisture products as much as possible. To produce a soil moisture data set with high spatial and temporal resolution, the similarity of microwave sensors must be considered, and the high-resolution visible light and thermal infrared data must be synchronized as much as possible. Few satellites meet these conditions at the same time. The Aqua satellite, which is equipped with both the Advanced Microwave Scanning Radiometer-Earth Observing System (AMSR-E) and the Moderate Resolution Imaging Spectroradiometer (MODIS) sensors, can simultaneously provide coarse-resolution passive microwave SM and LST/NDVI data, ~~providing a guarantee~~ guaranteeing that the data were acquired at the same time. However, AMSR-E data alone are insufficient (the instrument stopped working in October 2011); ~~and~~ thus, ~~we used~~ its successor AMSR2 can be used to continue the data series. The missing data between AMSR-E and AMSR2 (from November 2011 to June 2012) ~~is~~ can also be supplemented by SMOS-IC data, which ~~has~~ have been ~~verified~~ validated with ~~to have higher~~ high accuracy by using in situ measurements ~~across~~ around the ~~global~~ world (Al-Yaari et al., 2019; Ma et al., 2019).

In this study, in order to obtain a SM dataset with higher spatio-temporal resolution and higher consistency, all microwave SM data are based on AMSR-E Level 3 data, uniformly corrected to the same time and the same depth of detection using a linear regression method. In addition, ground station data are incorporated, and a large area of missing and invalid pixels is restored, so that the entire dataset is guaranteed to be complete in the Chinese region. A spatial downscaling method, namely, the spatial weight decomposition (SWD) model, was utilized to decompose the inconsistencies in soil depth and time in the coarse spatial resolution SM products with the TVDI into SM data with ~~a~~ 0.05° spatial resolution. The dataset covers the period from 2002 to 2018 and is comprehensively compared with in situ SM datasets.

2 Study area

~~Most of the areas in China, which~~ China is located within the central and eastern parts of Asia, ~~and~~ is situated along the western coast of the Pacific Ocean, ~~are~~ is affected by ~~the~~ a monsoon climate, which ~~and~~ ~~have significant~~ has important monsoon climate characteristics (Feng et al., 2003). Drought disasters in China have constantly increased over ~~the past few~~ recent years, ~~and drought~~ which has become one of the most serious types of natural disasters. Rapid increases in industrial, irrigation and domestic water use have resulted in dramatic increases in water resource consumption, which in turn have led to a significant increase in droughts in much of China, especially northern China (Zhao, et al., 2017). Thus, there is an urgent need to improve our knowledge about the spatial and temporal variability of SM ~~in order~~ to provide a basis for quantification and prediction, especially for the management of agricultural water (Liu, et al., 2012). Hence,~~ it is necessary to~~ constructing a set of high-precision and high spatial resolution SM datasets in China is necessary.

To ~~study~~ improve the quality of SM dataset and explore the spatial and temporal patterns of SM throughout the various regions of China, we further divided China into six regions ~~according~~ based on conditions such as elevation, rainfall, topography and hydrogeology combining hydrogeologic features: Northeast Monsoon Region (NEM), North China Monsoon Region (NCM), South China Monsoon Region (SCM), Southwest Humid Region (SWH), Northwest Arid Region (NWA), and Qinghai-Tibet Plateau Region (QTP) (Liang, et al., 2017). The ~~Northeast Monsoon Region~~ NEM includes the areas to the south of the Heilongjiang River, to the east of the Daxinganling Mountain range and to the north of the Ming Great Wall (117-135 °E, 38-53 °N), . The North China Monsoon Region, which extends from the Inner Mongolia Plateau to the northern part of the Qinling-Huaihe River, east to the eastern part of the Yellow Sea and the Bohai Sea, and west to the eastern part of the Qinghai-Tibet Plateau, has typical temperate monsoon climate characteristics (103-125 °E, 33-42 °N). The South China Monsoon Region includes the monsoon region to the east of the Yunnan-Guizhou Plateau and to the south of the Qinling Mountains-Huaihe River; this region has abundant rainfall and dense river networks and is characterized by a typical subtropical monsoon climate (20-33 °E, 105-123 °N). The Southwest ~~Wet~~ Humid Region includes the Qinghai-Tibet Plateau and the Yunnan-Guizhou Plateau to the south of the Huaihe River and the Sichuan Basin; precipitation is abundant in southwestern China (21-34 °E, 97-104 °N). The Northwest Arid Region includes the Inner Mongolia Plateau to the east of the Greater Xing'an Mountains and the vast arid and semiarid regions of Northwest China in the Tarim Basin to the north of the Qinghai-Tibet Plateau (73–126 °E, 37–55 °N). The Qinghai-Tibet Plateau Region includes the southern part of the Kunlun Mountains-Altun Mountains-Qilian Mountains, the area to the west of the Hengduan Mountains, and the entire Qinghai-Tibet Plateau to the north of the Himalayas (73–104 °E, 27–40 °N)~~,~~ (Zhao and Chen 2011). The locations of the meteorological stations and six geographic-climatic regions in China are shown in Figure 1. ~~For each region, we analyzed the current SM conditions and their changes over the past 17 years.~~

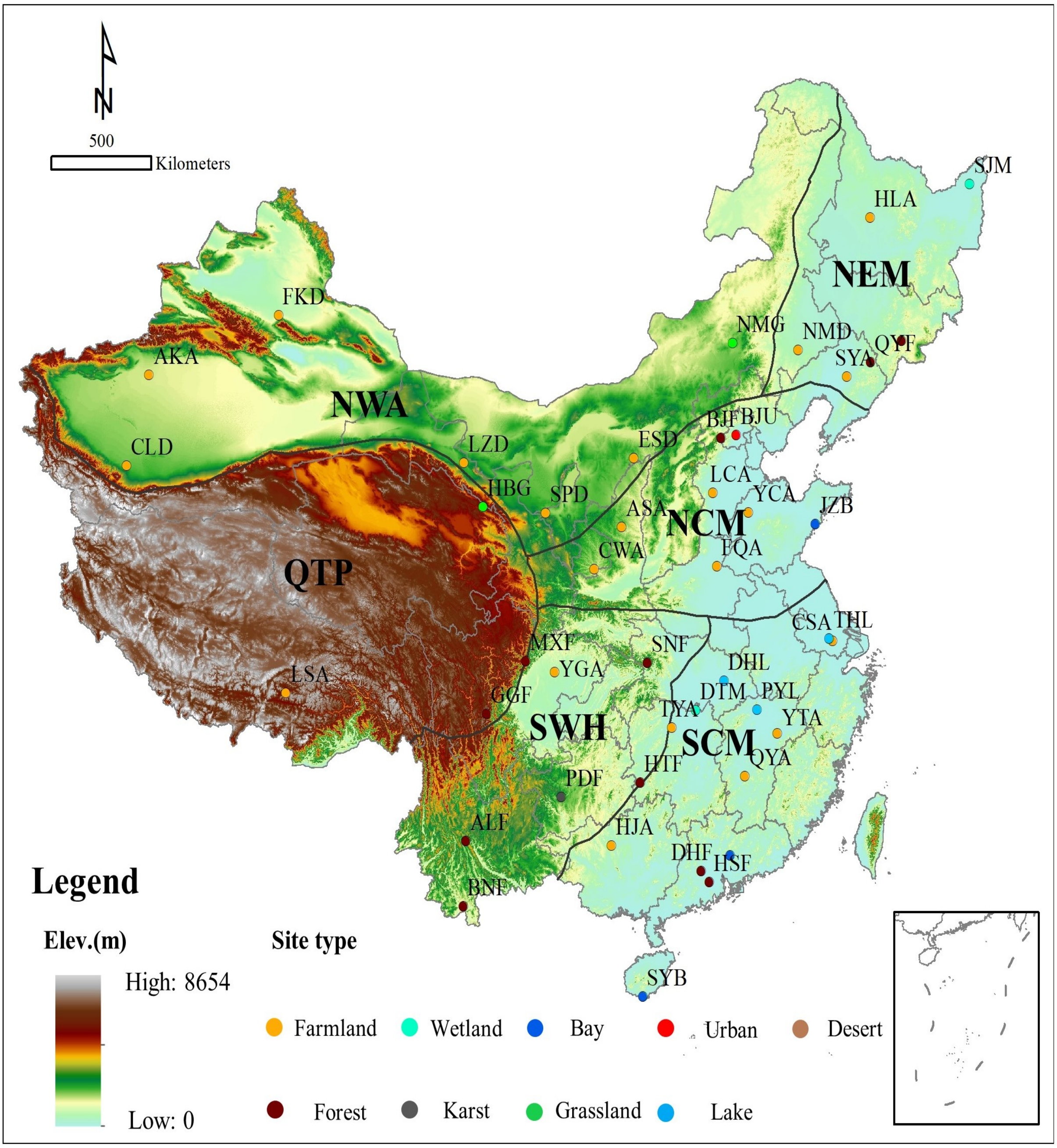
500
Kilometers
SJM
HLA
NEM
FKD
NMG
NMD
QYF
SYA
AKA
NWA
BJF
BJU
ESD
CLD
LZD
LCA
YCA
JZB
HBG
SPD
ASA
NCM
CWA
FQA
QTP
CSA
THL
MXF
SNF
DHL
YGA
LSA
GGF
DTM
PYL
TYA
YTA
SWH
SCM
QYA
HTF
PDF
HJA
ALF
DHF
HSF
Legend
BNF
Elev.(m)
Site type
SYB
High: 8654
Low: 0
Farmland
Wetland
Bay
Urban
Desert
Forest
Karst
Grassland
Lake

~~delete~~

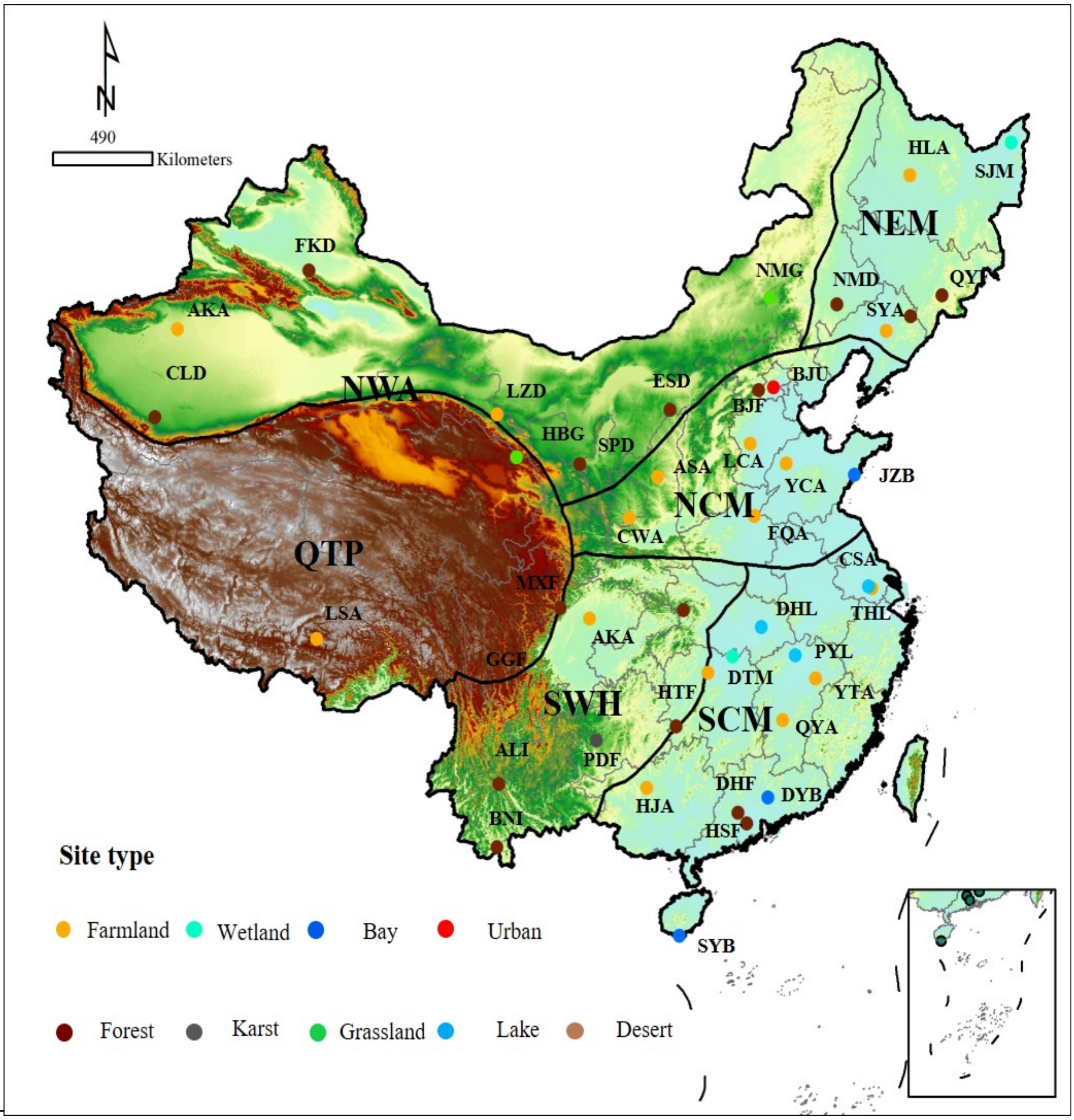
490
Kilometers
FKD
AKA
CLD
NWA
LZD
HBG
SPD
ESD
NMG
HLA
SJM
NEM
NMD
QYF
SYA
BJU
BJF
ASA
LCA
YCA
JZB
NCM
CWA
FQA
QTP
MXF
LSA
GGF
AKA
SWH
ALI
PDF
BNF
HTF
SCM
DTM
DHL
PYL
YTA
QYA
CSA
THL
HJA
DHF
DYB
HSF
SYB
Site type
Farmland
Wetland
Bay
Urban
Forest
Karst
Grassland
Lake
Desert

~~delete~~

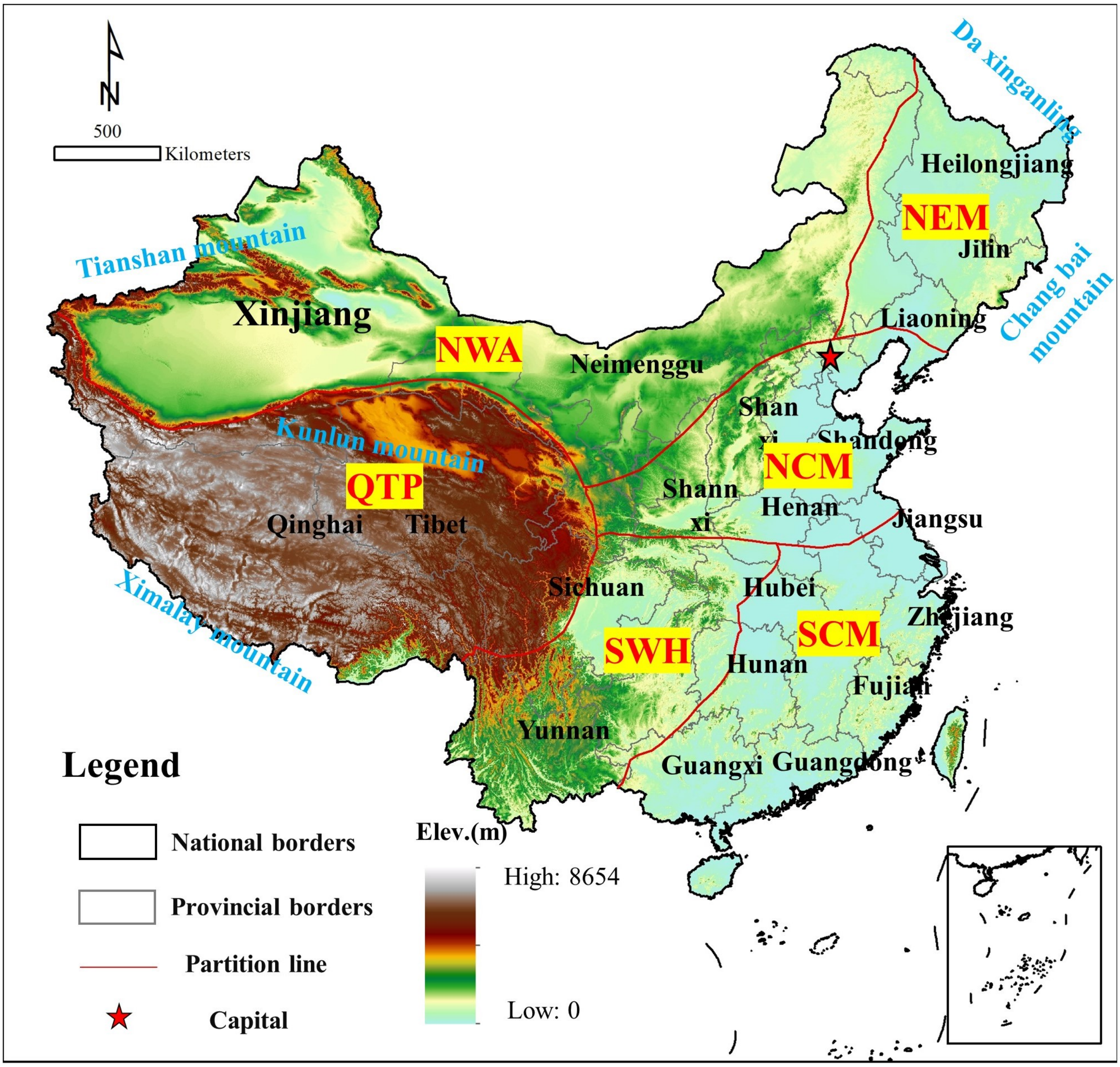

Figure 1: Overview of the study area, ~~location of the meteorological stations~~ and six geographic-climatic regions in China

~~Note: More detailed information on dense sites can be found in Table S1. Base map~~ The base map is derived from the Resource and Environment Science and Data Center of the Chinese Academy of Sciences (http://www.resdc.cn/, last access: 16 November 2019)

3 Data and methodology

3.1. Satellite-derived SM data

Since satellite sensors have a ~~finite working life~~ limited lifespan, to obtain a longer sequence of SM data sets, we need to use different satellite sensors to generate unbroken SM products. The SM data are mainly derived from the AMSR-E/2 Level 3 and SMOS-IC, ~~which have moisture units of m³/m³ and~~ with a spatial resolutions of 0.25°. ~~Among these satellite sensors,~~ AMSR-E is aboard the Aqua satellite (effective service period from May 2002 to October 2011) with transit times of 13:30 and 01:30, and the orbit is a sun-synchronous near-polar orbit with an orbital height of approximately 700 km (Kim, et al., 2012; Rüdiger et al., 2009)~~.~~ , which ~~AMSR-E~~ has six wavelengths in the microwave spectrum (6.925, 10.65, 18.7, 23.8, 36.5, and 89 GHz). The SM data utilized in the current research were obtained from the Japan Aerospace Exploration Agency

(JAXA) AMSR-E SM L3 product (Koike et al., 2004), and the time series ranges from July 2002 to September 2011. This product is based on the JAXA algorithm, and posted ~~on~~ with a 0.25° spatial resolution. First, a forward radiative transfer scheme is used to establish a brightness temperature dataset for a variety of frequencies and polarization-generated parameter values (soil and vegetation). Then, the brightness temperature dataset is used to create a lookup table (LUT). Finally, the SM and vegetation water content are estimated by using the microwave polarization difference index (MPDI) at 10.65 GHz and the index of soil wetness (ISW) at 36.5 GHz and 10.65 GHz horizontal channels (Koike et al. 1996, 2004). The JAXA algorithm assumes that the optical depth of vegetation is linearly related to the vegetation water content and that the vegetation water content can be determined by the NDVI. Based on ~~the~~ verification ~~of~~ with the ground monitoring network, JAXA products provide acceptable SM results (Zeng et al. 2015).

The AMSR2 sensor is mounted on the Japanese Global Change Observation Mission – Water Satellite 1 (GCOM-W1) and was launched in May 2012. As a follow-up to AMSR-E, AMSR2 has a larger antenna reflector diameter, increasing from 1.6 m to 2.0 m. Moreover, AMSR2 includes an extra C-band channel (with a frequency of 7.3 GHz) to mitigate radio frequency interference (RFI). The transit times are still 13:30 and 01:30. The data were derived from the JAXA SM products, which were released in real time, and the time span ranges from July 2012 to December 2018. As a continuation of the AMSR-E product, the AMSR2 L3 product also uses ~~an~~ a LUT method to obtain SM retrievals, providing two products with spatial resolutions of 0.1° and 0.25°. To better match the available data, this paper selects the data with a spatial of 0.25° ~~spatial resolution data~~. The accuracy of the JAXA AMSR2 product was verified to have a root mean square error (RMSE) of less than 0.06 m^3/m^3 (for a vegetation water content of $\leq$1.5 kg/m^2, Kim, et al. 2015).

The SMOS satellite was launched on 2 November ~~2,~~ 2009~~.~~, which ~~This satellite~~ travels along a sun-synchronous orbit with an average altitude of 758 km and a dip of 98.44°. The transit times are approximately 06:00 (ascending) and 18:00 (descending) local time with a two- to three-day revisit frequency. The operating L-band (1.4 GHz), measured with a Microwave Imaging Radiometer with Aperture Synthesis (MIRAS), is used to observe SM (Kerr et al., 2012; Lacava, et al., 2012; González-Zamora et al., 2015). This study uses the SMOS-IC V105 SM product contributions from the Centre Aval de Traitement des Données SMOS (CATDS), with a time series ranging from October 2011 to June 2012 and a spatial resolution of 25 km. The SMOS-IC algorithm was designed by the Institut National de la Recherche Agronomique (INRA) and Centre d'Etudes Spatiales de la BIOsphère (CESBIO) (Fernandez-Moran et al., 2017). The SMOS-IC product was further quality filtered and redivided based on the previous SMOS Level 2 SM user data product (SMDUP2) algorithm. That is, the values of the grid point data quality index (DQX) greater than 0.07, which were affected by RFI or SM, were discarded; then, the DQX reverse-weighted average was used to group the SMDUP2 data on a 0.25° equal-area grid and obtain SMOS-IC-grade products with a 25 km spatial resolution. Al-Yaari et al. (2019) and Ma et al. (2019) conducted comprehensive ~~evaluation~~ evaluations of the SMOS-IC SM product by using ground measurements worldwide. The results showed that the SMOS-IC SM product agreed better with in situ measurements than other SMOS products (SMOS L2 and L3). The SMOS-IC scientific data were as independent as possible from auxiliary data, and the data are available at https://www.catds.fr/Products/Available-products-from-CEC-SM/SMOS-IC. The data are provided on a daily time scale to match the AMSR-E/2 L3 SM products at the same scale. The SMOS-IC SM data were aggregated to a monthly temporal resolution.

3.2 MODIS LST and NDVI data

In a downscaling model, ~~it is critical to~~ establishing the relationships between SM and other high-resolution surface variables is critical. Im et al. (2016) utilized the relationships between SM and MODIS-derived products to improve the resolution of the AMSR-E SM product. Wang et al. (2016) downscaled SM data from a 0.25° resolution to a 0.05° resolution using a similar approach. Zhao et al. (2018) used the vegetation-thermal relationship to establish a microwave-optical/infrared downscaling model to optimize the spatial resolution of SMAP SM products to a very good level of precision. All these land surface variables are available from the corresponding MODIS products. The MODIS sensor aboard the Aqua satellites passes over China at approximately 01:30 (descending) and 13:30 (ascending). MODIS has been widely used to monitor various environments, including land, oceans, and the lower atmosphere, due to its high temporal resolution and good data quality. In this study, two MODIS products were used, namely, the MODIS/AQUA monthly LST (MYD11C3) and NDVI (MYD1C2) products, which have 0.05° spatial resolutions, to ensure the same transit time as the microwave SM data. The MODIS products were downloaded from the NASA Land Processes Distributed Active Archive Center (LPDAAC) ~~from~~ at the United States Geological Survey (USGS) (https://lpdaac.usgs.gov/). ~~To be~~ For consistency ~~consistent~~ with the SM data, all data were averaged by day and night products, and outliers were eliminated by the first-order difference method. Furthermore, null values were interpolated using the Savitzky-Golay filter.

3.3 Meteorological and ~~Auxiliary Data~~ auxiliary data

SM data from the China National Meteorological Station (CNMS) and China's agrometeorological and ecological observation network (http://data.cma.cn/, last access: 16 November 2019) were used to ~~verify~~ validate the ~~downscaling~~ downscaled SM products. We used the hourly in situ ~~soil moisture~~ SM data measured at 0-10 cm depth to investigate the accuracy of the satellite-derived surface SM estimates. Monthly products were obtained from ~~the~~ 2420 agrometeorological stations (including the Key station/National Climate Observatory, Basic station/National Meteorological Observatory and General-station/regional meteorological station). Based on the nearest neighbor data during the daily satellite transit, and aggregated into monthly products through ~~average~~ averages to match the satellite ~~downscaling soil moisture~~ downscaled SM products; see Figure A1 for site space ~~location~~ locations. ~~Take the~~ The AMSR series satellites used in this research is taken as an example. The daily transit times of the satellites in China ~~is~~ are 13:30 and 1:30. Therefore, the ground ~~soil moisture~~ SM measurements ~~at the~~ in daytime (13:00 and, 14:00) and ~~the~~ nighttime (1:00 and, 2:00) are averaged. In the aggregation calculation, abnormal and unrepresentative data are eliminated to ensure that the selected data can reflect all the physical conditions that affect the remote sensing signal. The China Ecosystem Research Network (CERN) ~~are~~ has locations in different regions of the study area ~~(Figure 1)~~ and ~~represent~~ records different surface and climatic conditions, which ~~were~~ are used to ~~validate~~ validate the downscaled SM deviation in different land cover types.

In addition to the above data, the Shuttle Radar Topography Mission (SRTM) ~~Land Precesses Distributed Active Archive Center (LPDAAC)~~ of the USGS (https://lpdaac.usgs.gov/) provides digital elevation model (DEM) data with a resolution of 1 km resampled to 0.05°. These data were used to obtain terrain factors (e.g., elevation and slope) for the downscaling studies. The TRMM 3B43 precipitation and Chen et al. (2021) developed a global remote sensing-based surface soil moisture (RSSSM) dataset ~~are used~~ to assist in assessing the quality of downscaled products. Table 1 describes lists an overview of the main data sets and a description of the corresponding variables for each data set in this study. According to the seasonal division of weather, spring ranges from March to May, summer from June to August, autumn from September to November, and winter from December to February.

Table 1: Overview of the data sets used in this study.

Data sets	Satellite	Spatial/temporal resolution	Dates	Description
AMSR-E L3	Aqua	0.25°/1 month	2002/07-2011/10	SM
SMOS-IC	SMOS	0.25°/1 month	2011/10-2012/06	SM
AMSR2 L3	GCOM-W1	0.25°/1 month	2012/07-2018/12	SM
MOD11C3	Aqua	0.05°/1 month	2002/07-2012/12	LST
MOD13C2	Aqua	0.05°/1 month	2002/07-2018/12	NDVI
TRMM 3B43	TRMM	0.25°/1 month	2002/07-2018/12	Precipitation
RSSSM	-	0.1/10 days	2003/01-2018/12	SM
SRTM	-	Resample 0.05°	-	DEM, slope
Station	-	1 day	2002/01/01-2018/12/31	SM

3.4 Methodology

3.4.1 Calibration and restoration of the satellite-derived SM

~~Microwave~~ The microwave frequency and overpass time of the satellite are two important factors for deriving SM values (Cashion, et al., 2005). In theory, the surface SM data retrieved from different frequencies have different soil sampling depths (Njoku, et al. 2003). ~~Because the~~ The diurnal variations in SM and temperature may be considerable in some regions, so the the overpass time of the sensor can influence the retrieved SM. AMSR-E and AMSR2 have the same ascending/descending overpass times, i.e., 13:30 ~~p.m.~~ and 1:30 ~~a.m.~~ local time. The SMOS SM retrievals occur at dawn and nightfall, corresponding to the SMOS ascending/descending overpass times at 6:00 ~~a.m.~~ and 18:00 ~~6:00 p.m~~. Differences in the overpass time and observed depth of the sensors could be serious issues when matching data, particularly when deriving long-term trends. Hence, the impact of differences among sensors is considered in this study. ~~Despite soil moisture~~ Although SM measurements retrieved from AMSR-E/2 and SMOS ~~having~~ have some differences ~~absolute values~~, they show similar seasonal patterns, which provides the possibility for calibrating and rescaling to yield a long-term dataset. AMSR-E was selected as the reference in this study because it is associated with a relatively long time series. ~~The monthly SM average is calculated from the use of~~

~~more than one and half months~~. The linear regression matching technique was chosen as the ~~calibrating~~ calibration method. Similar matching approaches have been successfully used in the past (e.g., Crow and Zhan, 2007). Crow and Zhan (2007) rescaled satellite SM observations with a model by linear regression matching, and Brocca (2013) also established regression relationships between satellites and in situ observations for calibration of satellite SM observations ~~of SM~~ using regression matching. In general, the linear rescaling method is realized by considering the most general linear relationship between the reference dataset (X) and the original dataset (Y). In this study, the linear regression method ~~was~~ is applied cell by cell and its form is Eq. (1):

$$Y^* = \mu_X - (Y+\mu_Y)C_Y \tag{1}$$

where μ_X and μ_Y are the average values of X and Y to calculate the sequence respectively~~,~~; Y^* is the scaled value of the original data Y~~,~~; and C_Y is a scalar scaling factor~~, .and in~~ In this study, we eliminate the largest-smallest impact in the fitting process. Here is a linear method proposed by Yilmaz and Crow (2013) to determine the size of C_Y. ~~The~~ C_Y ~~was~~ is calculated via Eq. (2)

$$C_Y = \rho_{XY}\sigma_X\sigma_Y \tag{2}$$

where ρ_{XY} is the correlation coefficient of X and Y, and σ_X and σ_Y are the standard errors of X and Y, respectively.

The calibration procedure ~~was~~ is applied to monthly averages of SMOS-IC data. The SMOS-IC values are plotted against the AMSR-E values for the overlapping period (07/2002 to 10/2011) to calculate ~~calibrating~~ calibrated parameters (linear equations). ~~Second~~, Next, the calibrating equations derived from the previous step are applied to SMOS-IC data for the period from 2011 through 2012, producing calibrated SMOS data (SMOS $_{reg}$ refers to the calibrated values). The AMSR2 values are calibrated against the SMOS-IC values using data from the overlapping period. The equations derived from the previous step are used to calibrate the AMSR2 data from the period 2012 through 2018, producing AMSR2 $_{reg}$. The AMSR-E, SMOS $_{reg}$, and AMSR2 $_{reg}$ data are thus obtained from 2002 to 2018.

3.4.2 Downscaling method ~~of~~ for SM

Based on the identification of a negative correlation between the SM products and LST/NDVI, we construct a relatively simple and efficient ~~downscaled~~ downscaling process, in which the TVDI is a weighting factor for downscaling. First, we computed the fault and null value areas based on the Savitzky-Golay filter to eliminate the effects of clouds and water vapor on the MODIS LST/NDVI images. Then, we ~~built~~ build an LST terrain correction model to reduce the influence of terrain fluctuations on the surface temperature inversion results. In addition, we ~~established~~ establish a monthly TVDI distribution using the LST/NDVI inversion model based on LST and NDVI images acquired from MODIS with 0.05° spatial resolution. Finally, we ~~constructed~~ construct an SWD model to decompose the SM pixel by pixel and generate a monthly 0.05° SM gridded product. ~~The structure~~ A structural diagram of the method is given in Figure 2.

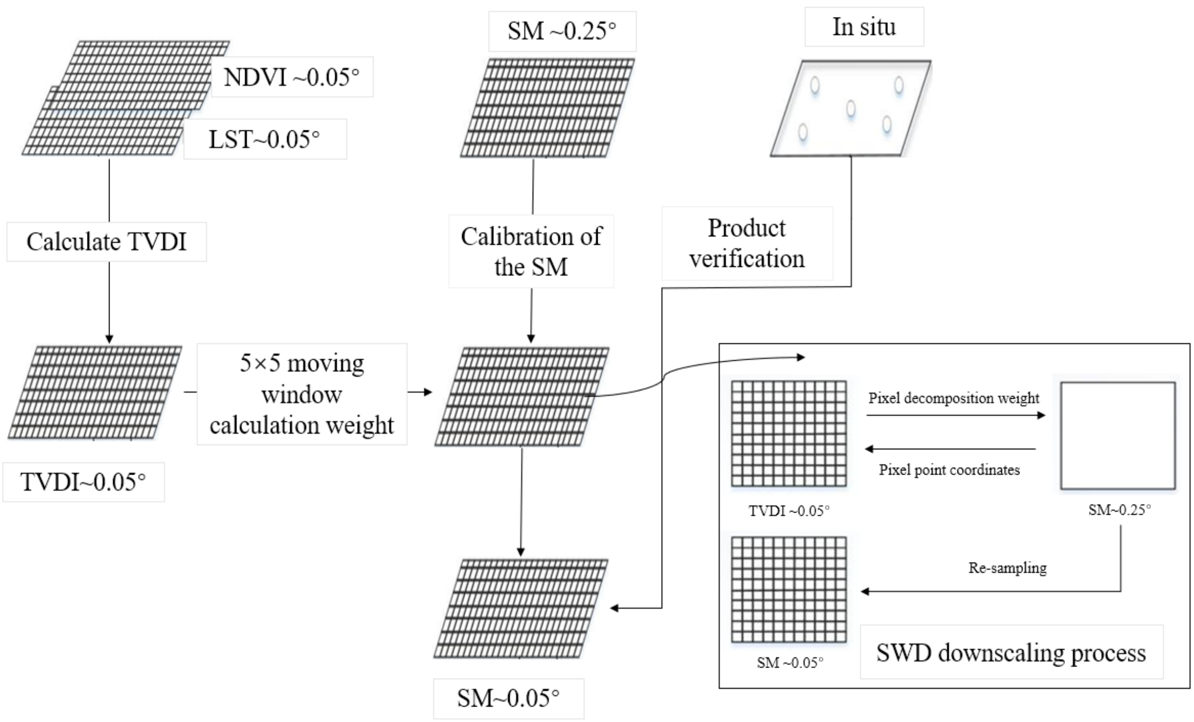

Figure 2: The flowchart for the fine SM dataset

Since ~~optical data will be~~ are ~~affected by clouds and harsh atmospheric conditions, there are missing and discontinuous~~ visible light and thermal infrared remote sensing are greatly affected by clouds and harsh atmospheric conditions, there is a lack of continuous LST and NDVI data. To compensate for the error caused by insufficient MODIS data, the first-order difference method is used to eliminate outliers, and ~~then~~ the Savitzky-Golay (S-G) filter is then used to reconstruct the time series data from 2002 to 2018, and to interpolate the null values of the missing data. The specific method is shown in Eq. (3):

$$Y_j^* = \sum_{-m}^{m} \frac{C_i * Y_{j+1}}{N} \tag{3}$$

where Y_j^* represents the time series data after the supplementation; Y_{j+1}^* is equal to half the size of the smoothing window; C_i is the fitting coefficient of the Savitzky-Golay polynomial filter, i.e., the weight of the *i-th* value from the filter head; and N is the length of the data processed by the filter (the number of data points contained in the sliding window).

Due to the large elevation variations in China, the influence of terrain on temperature must be corrected before the TVDI can be calculated. To reduce the influence of terrain fluctuations on the surface temperature data, Eq. (4) is used to correct the LST products acquired from MODIS, as described in previous studies (Molero et al., 2016):

$$T_m = T_o + \hbar \times \lambda \tag{4}$$

where T_m is the corrected surface temperature, T_o is the surface temperature before correction, h is the elevation value at a certain pixel, and λ is the average influence coefficient of the elevation on the surface temperature inversion process (where the best value of λ is 0.006 °C/km).

The TVDI calculation formula, which was proposed by Sandholt (2002), can adequately estimate the surface water conditions of soil. Thus, the TVDI has been widely used in drought monitoring, and the TVDI expression is shown in Eq. (5), (6) and (7):

$$TVDI=\frac{T_s\text{-}T_{s\,min}}{T_{s\,max}\text{-}T_{s\,min}} \tag{5}$$

$$T_{s\,max}=a_1+b_1*NDVI \tag{6}$$

$$T_{s\,min} = a_2 + b_2 * NDVI \tag{7}$$

where T_s is the LST (°C) in the study area, T_{smin} is the LST of the wet side, (a_2, b_2) is the simulation coefficient of the "wet edge" model, T_{smax} is the surface temperature of the dry side and (a_1, b_1) is the simulation coefficient of the "dry edge" model.

Based on the LST/NDVI feature space, many studies have shown that the TVDI exhibits a significant negative correlation with SM (Wang, 2016). The high-resolution TVDI distribution is used to weight the low-resolution SM data pixel by pixel; then, the weight is used to decompose the low spatial resolution SM product into 0.05°SM products. The SWD ~~Eq. (8) is as follows~~ is computed by Eq.(8):

$$SM_i = SM_j \times \frac{1-TVDI_a}{1-TVDI_b} \tag{8}$$

where SM_i represents the downscaled *SM* ~~data used to generate the~~ with 0.05° pixels, SM_j represents the input low-resolution microwave SM ~~data~~ with 0.25° pixels, $TVDI_a$ is the TVDI value calculated using ~~of~~ the MODIS ~~pixels corresponding to the SM in pixel *a*~~, and $TVDI_b$ is the TVDI average ~~of the~~ MODIS pixels corresponding to the ~~SM in pixel *b*~~ area of microwave observations of SM.

3.4.3 Evaluation metrics of downscaled SM

It is necessary to evaluate the SM downscaling results before further application. The accuracy of the fine spatial resolution SM is evaluated in terms of *R*, ~~root mean square error (RMSE),~~ bias and unbiased RMSE (ubRMSE) (Ma et al., 2019). ~~For this purpose, the Taylor's diagram is used to statistically summarize the correlation coefficient, centered RMSE (*E*), and normalized standard deviation (SDV) of the simulation results from the site observations by a single point in two dimensions (2-D). The error metrics used in the study are defined as follows:~~

$$R = \frac{1}{N-1}\sum_{i=1}^{N}(\frac{T_i-T}{\sigma_T})(\frac{L_i-L}{\sigma_L}) \tag{9}$$

$$Bias = \frac{1}{N}\sum_{i=1}^{N}(T_i - L_i) \tag{10}$$

$$RMSE = \sqrt{\frac{1}{N}\sum_{i=1}^{N}(T_i - L_i)^2} \tag{11}$$

$$ubRMSE = \sqrt{RMSE^2 - Bias^2} \tag{12}$$

$$\cancel{E^2 = SDV^2 + 1 - 2SDV \times R} \tag{13}$$

~~Correspondingly, *E* can also be defined as:~~

$$E = \sqrt{\frac{ubRMSE^2}{\sigma_L}} \tag{14}$$

~~where~~

$$SDV = \frac{\sigma_T}{\sigma_L} \tag{15}$$

where T_i is the downscaled SM value in the *i-th* year, L_i is the in situ SM value in the *i-th* year; T and L are the mean downscaled and in-situ SM values, respectively; N represents the total number of observations; and σ_T and σ_L represent the standard deviations of the downscaled and in-situ SM values, respectively.

~~In the Taylor diagram, the SDV and *R* are expressed as the radial distance and the angle in the polar plot, respectively. Therefore, *E* represents the distance of the point "observed" on the Taylor diagram. The shorter the distance, the better the consistency between the tested LST product and the reference LST observation. Only significant correlations were considered in this study (p-value < 0.05).~~

4 Results

4.1 Verification of the downscaled soil moisture datasets

Figure A2 shows the ~~soil moisture~~ SM images before and after downscaling in June 2002 and the value of a cross-sectional pixel. The results of downscaled SM products using spatial weights better retain the spatial distribution of the original images. Specifically, the spatial details of the ~~soil moisture~~ SM data after downscaling are ~~more delicate~~ finer. ~~It is very important to validate the SM product before application.~~ ~~Because monthly products were produced in this study, we verified~~ ~~validated~~ ~~these products on monthly, seasonal and annual scales. Based on a comparison of the remote sensing data with the ground agricultural meteorological stations data, the validation reveals that the downscaled SM products boast a high accuracy at the monthly, seasonal and annual scales (Figure 3).~~ Before applying the downscaled SM products, the high-spatial resolution downscaled SM productions are first validated against the in situ observations of CNMS over China, at three temporal scales. ~~The values of the ground-measured SM were all slightly higher than those of the downscaled SM. However, due to the high variability in the SM at the seasonal scale, measurements at the monthly and seasonal temporal scales did not show the temporal SM trends or the yearly averaged SM values. When compared with the ground measurements, the downscaled SM data underestimated the ground observations at all three temporal scales, especially the monthly scale. We calculated the correlation coefficients (*R*) between the in situ and remotely sensed SM values; the *R* value was particularly high at the yearly scale. Specifically, at the monthly, seasonal and annual scales, the *R* values were approximately 0.84, 0.85, and 0.89 respectively; the corresponding ubRMSE were 0.051, 0.048 and 0.042 m^3/m^3 respectively. Additionally, the bias value was -0.016 m^3/m^3 on the annual scale, while the monthly and seasonal biases were -0.024 and -0.030 m^3/m^3, respectively.~~ Figure 3(a) displays the scatterplots between monthly downscaled SM and measured SM. ~~It can be easily seen that the~~ The downscaled SM agrees well with the ground-measured SM with a correlation coefficient (R) of 0.84, and the bias and *ub*RMSE are -0.057 m^3/m^3 and 0.056 m^3/m^3 respectively. Moreover, the comparisons at seasonal and annual temporal scales are also carried out (as shown in Figure 3 (b) and (c), respectively). Slightly better than monthly scale results are observed with R, bias, and *ub*RMSE, ranging from 0.85 to 0.89, from −0.063 m^3/m^3 to -0.027 m^3/m^3, and from 0.036 m^3/m^3 to 0.048 m^3/m^3, respectively.

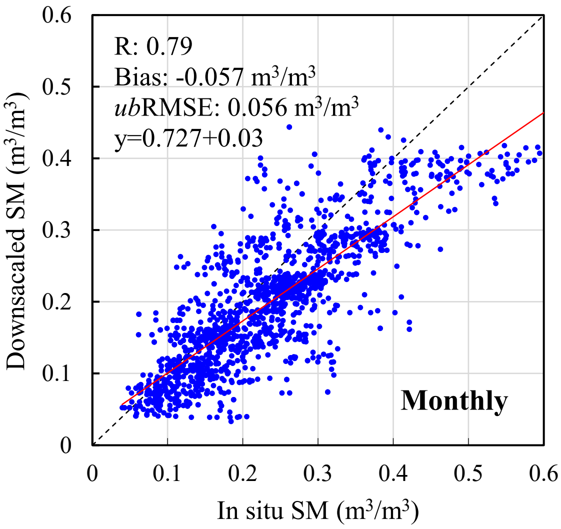

(a)

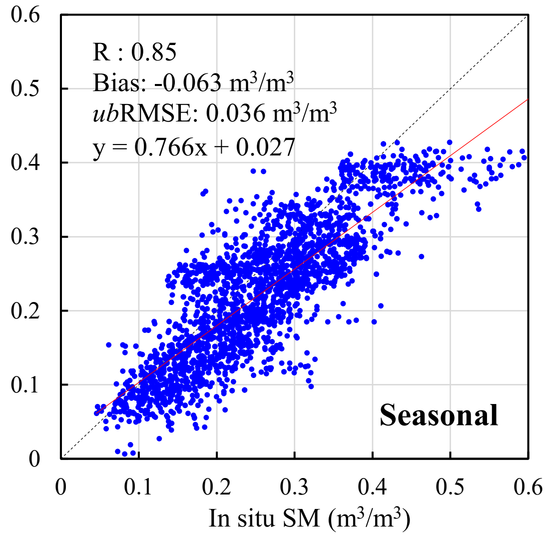

(b)

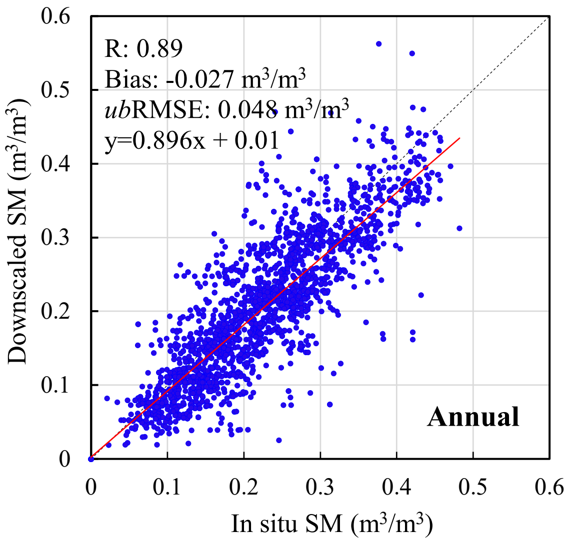

(c)

Figure 3: Correlations between the downscaled SM and in situ SM measurements at the (a) monthly, (b) seasonal and (c) annual scales. The solid lines are the trend lines, and the dashed lines are the y=x reference lines.

~~The ubRMSE, bias and *R* results for the SM products in different areas were calculated using in situ SM data.~~ Although the downscaled SM products show a high accuracy level overall, we still need to further analyze the consistency of the downscaled SM and ground-measured SM in different regions. In Figure 4, the box plots present the median ~~of~~ for each indicator (the horizontal line within each box) and the first (Q1) and third quantiles (represented by the bottom and top of the box, respectively). The downscaled SM is strongly correlated with the in situ measurements, with mean R > 0. 64 during 12 months in the subregions. ~~with *R*> 0.52 at most times during the 12-month period.~~ Specifically, the downscaled SM products ~~had~~ have the lowest *R* and the highest bias and *ub*RMSE in December ~~(possibly attributable to ice and snow cover in winter)~~. The downscaled SM products ~~displayed~~ display the best correlation with in situ measurements in September (weaker vegetation impact). Compared to the values ~~of~~ in the North China Monsoon and Northeast Monsoon Regions, the deviation values ~~of~~ in the South China Monsoon and the Qinghai-Tibet Plateau Regions are more variable. The reasons for this variability ~~is~~ are not the same; on the Qinghai-Tibet Plateau, some regions ~~is~~ are covered by snow and ice around the year, while South China features dense surface water networks and abundant rain. ~~Please note~~ Note that~~,~~ the ~~soil moisture~~ SM data ~~of~~ for the frozen soil region ~~is~~ are somewhat questionable. ~~In order to~~ To maintain the integrity of the data and because a previous study demonstrated that the JAXA AMSR-E/2 products still have some ~~capability~~ ability to capture the temporal ~~tend~~ trend of ~~soil moisture~~ SM in frozen seasons (Zeng et al., 2015), we ~~keep it~~ retain these data. Therefore, the follow-up verification and analysis process also follow this criterion.

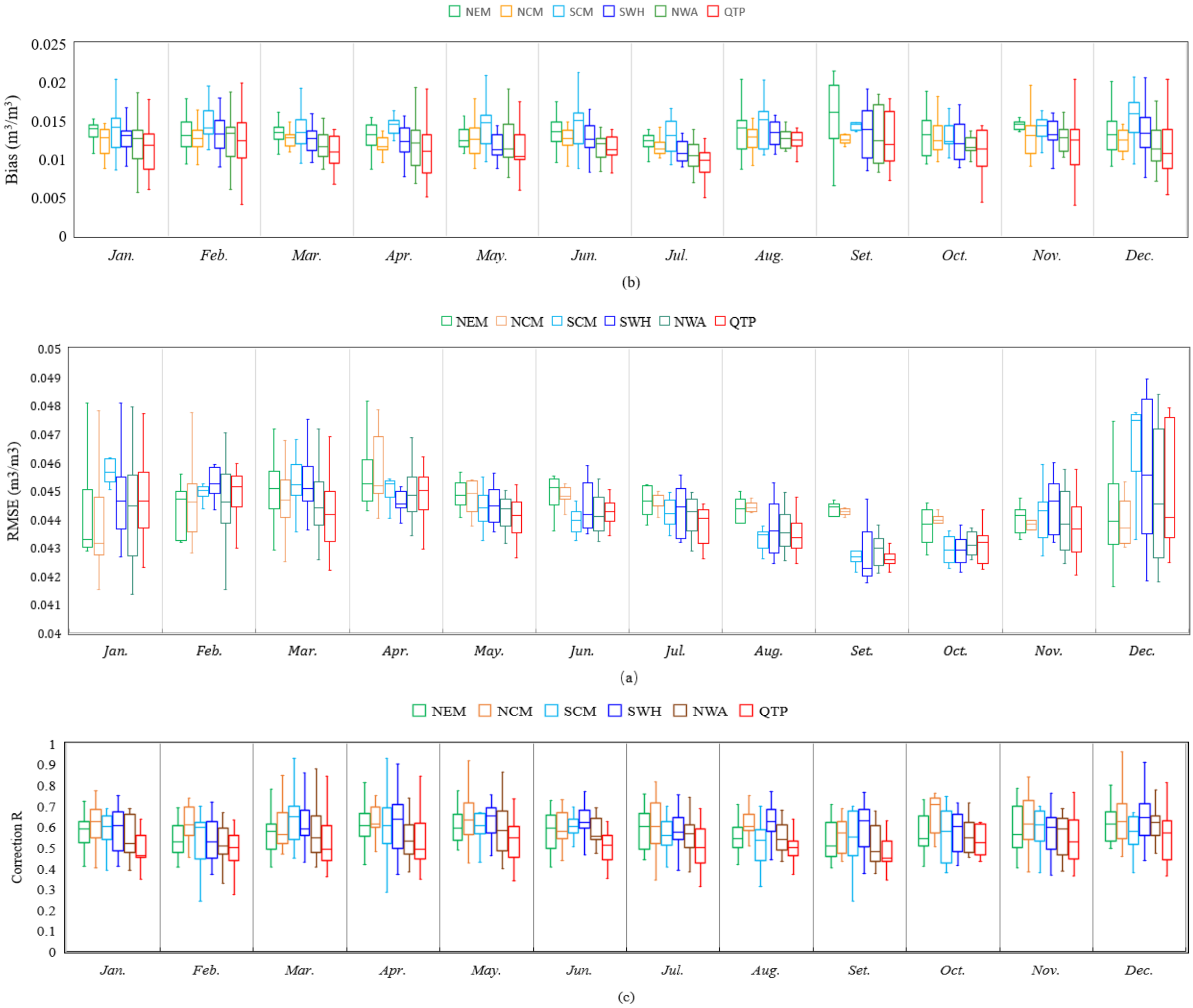

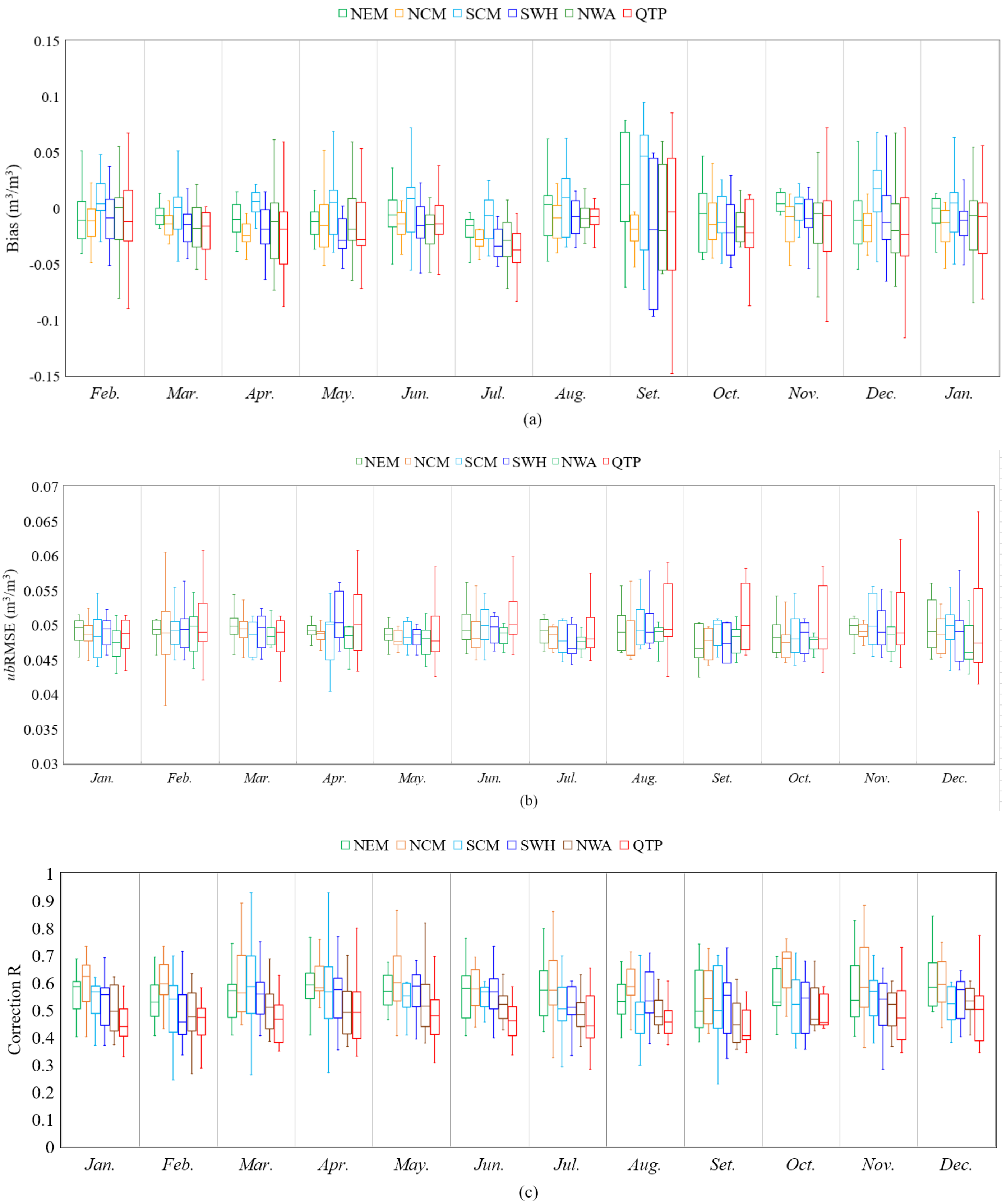

Figure 4: Box plots of the RMSE, bias and *R* (p<0.05) of comparison between downscaled SM and in situ SM in each region.

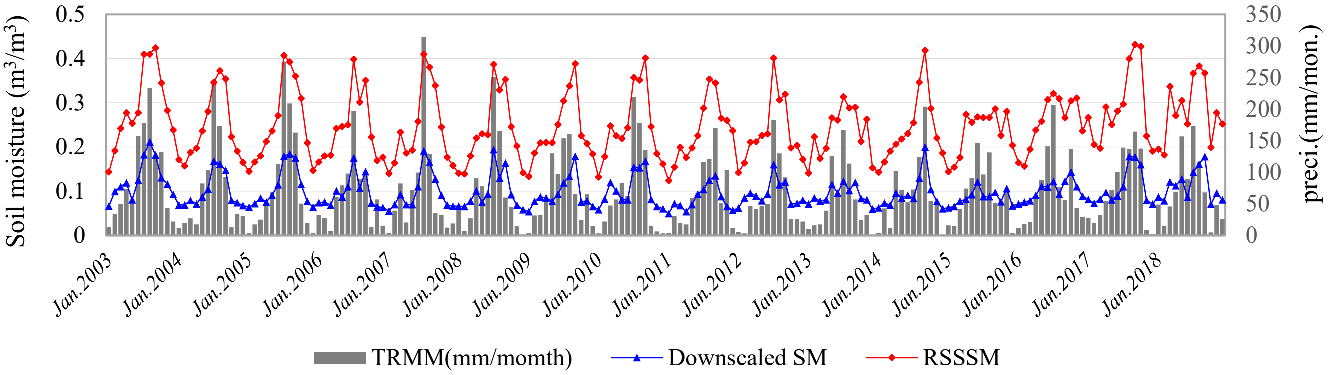

Figure 5 Time series of the area mean downscaled SM, RSSSM and TRMM precipitation during the study period from 2003 to 2018.

In addition, the time series of downscaled SM, RSSSM and TRMM precipitation are also explored. The analysis of Figure 5 shows that although the two groups of SM products differ greatly in absolute values due to their own algorithmic characteristics, they have a high degree of consistency in relative changes and are consistent with precipitation trends. Overall, the above results further demonstrate the validity of the downscaled SM, implying that the downscaled SM values are applicable for high-precision hydrology and drought monitoring applications.

~~As a complement to the evaluation presented in the previous section, the performance of the downscaled SM product was evaluated against in situ surface SM observations from stations in different land cover areas. The performance of the downscaled SM at the selected stations is provided, and the performance criteria (including *R*, SDV and center RMSE) estimated between the downscaled SM and in situ observations are also reported in Taylor diagrams in Figure 5. In general, the dots (stations) are unevenly distributed in the Taylor diagrams for all regions, indicating that the downscaled SM accuracy varies from one station to another. Forest land estimates more frequently plot outside of one normalized SDV circle than other estimates, indicating that SM associated with higher vegetation is more variable.~~

~~In eastern China (the Northeast Monsoon, North China Monsoon, and South China Monsoon Regions), the downscaled SM products are in good agreement with the ground observations, although the variability of a few stations is large. Most of the correlation (*R*) values between the downscaled SM and the in situ observation range between 0.6 and 0.9. In western China, i.e., the Qinghai-Tibet Plateau and the Northwest Arid Regions, the downscaled products have poor correlations with the in situ observations, but higher correlation values were generally obtained in low vegetation areas.~~

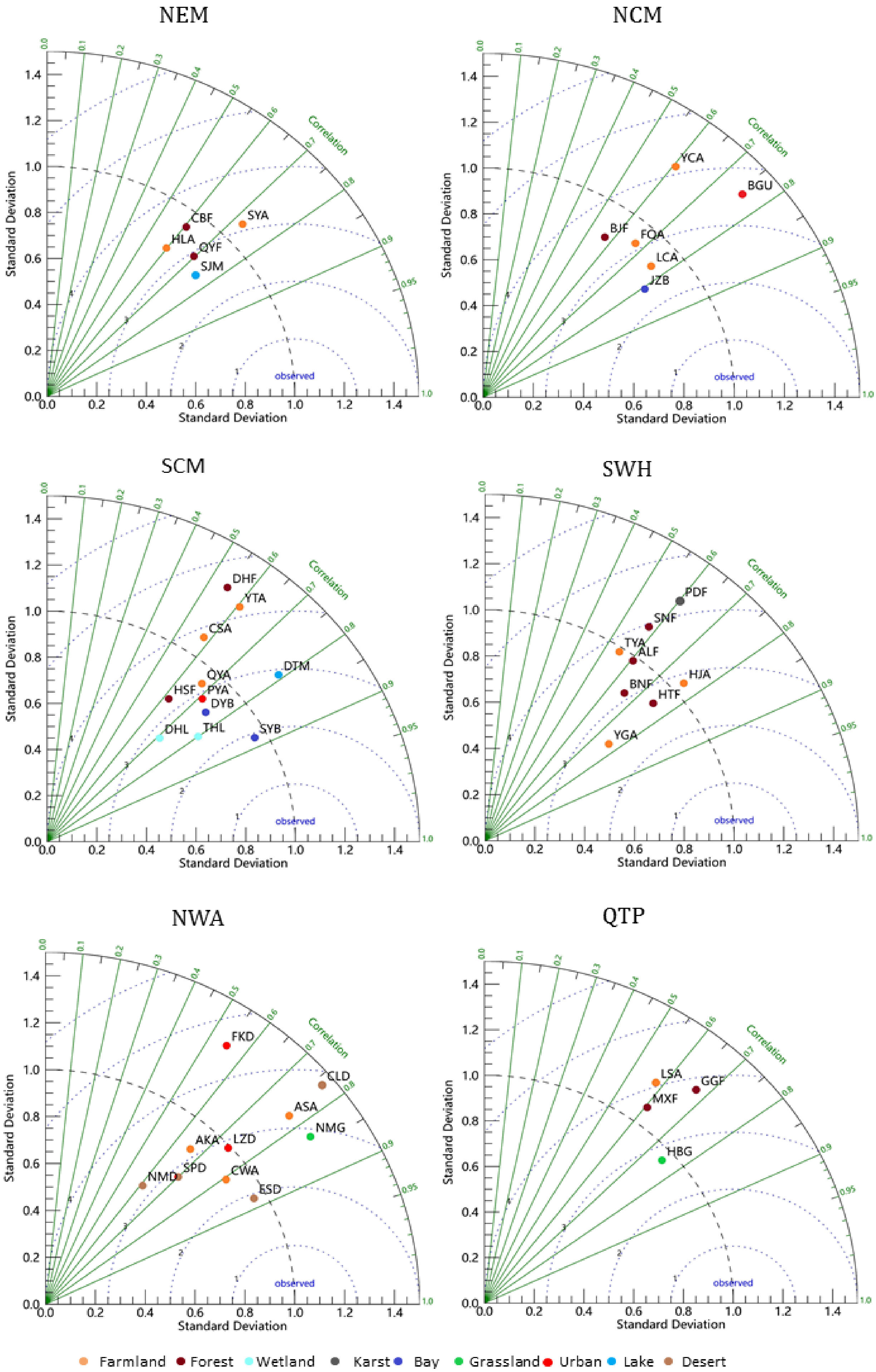

~~Figure 5: Taylor diagrams illustrating a statistical comparison between downscaled SM and in situ measurements in each region.~~

4.2 Spatiotemporal ~~change~~ changes in ~~of~~ SM in different natural regions of China

~~Over the past 17 years, the national average SM content was approximately 0.093m^3/m^3 and exhibited an overall decreasing trend (b = -0.167, R = 0.750, P = 0.05). This result also explains the increase in temperature, which resulted in an increase in evaporation and thus a decrease in SM in the context of global warming. From 2002 to 2012, there were slight fluctuations, but after 2013, the SM content sharply decreased. In addition, the years with the highest and lowest SM contents were 2004 (11.07%) and 2016 (7.31%), respectively. From the annually averaged SM content of each subregion over the past 17 years, the SM values in the South China Monsoon Region were much higher than those in the other regions (average of 16.46%). In this region, the values of 2002-2011 were consistent with the national average (Similar trend or similar values), and the values of 2011-2013 were higher than the national average. The significant decline in SM in this region shows that it was more affected by the monsoon than the other regions in China. In contrast, the average annual trends of the North China Monsoon Region and Northeast China Monsoon Region, which are also affected by the monsoon, were relatively stable. The Southwest Wet Region ranked second, with an average SM of 9.16%, followed by the Northeast Monsoon Region and the North China Monsoon Region, with average SM values of 8.69% and 8.44%, respectively. Furthermore, the Northwest Arid Region and the Qinghai-Tibet Plateau Region displayed consistently low SM averages of 6.87% and 6.34%, respectively. The accuracy of the SM products in the Qinghai-Tibet Plateau Region was relatively low, mainly due to the greater impact of snow cover. This analysis shows that the SM contents of monsoon-affected areas (i.e., the Northeast China Monsoon Region, North China Monsoon Region and South China Monsoon Region) are more sensitive than those of inland areas (Northwest Arid Region and Southwest Wet Region). The average SM content was highest in the South China Monsoon Region, which also showed the most significant change. This region displayed a decreasing trend throughout the study period. The rate of decline in this region is defined by (b= -0.246, R=0.570, P=0.01) and is much higher than the rates in the other monsoon regions. The North China Monsoon Region has experienced numerous droughts in the past and is currently exhibiting a decreasing trend (b=-0.383, R =0.621, P=0.05). Thus, it is predicted that the drought in North China will further intensify and even trigger a series of agricultural disasters. The SM contents in the Southwest Wet Region and the Northeast China Monsoon Region have slightly decreased over the past 17 years, but the Northwest Arid Region has shown a slight increasing trend (b=0.04, R=0.651, P=0.05). The drought situation in the northwestern part of the study area has positive significance for ecological, agricultural and livestock production in the Northwest Arid Region of China.~~

Figure 6 (a) shows that downscaled SM can represent the typical seasonal variations well, with minimum SM in winter and maximum SM in summer affected by the monsoon in China. The figure also illustrates that the downscaled SM captures the extreme drought events occurring in 2009, 2011 and 2015 well.

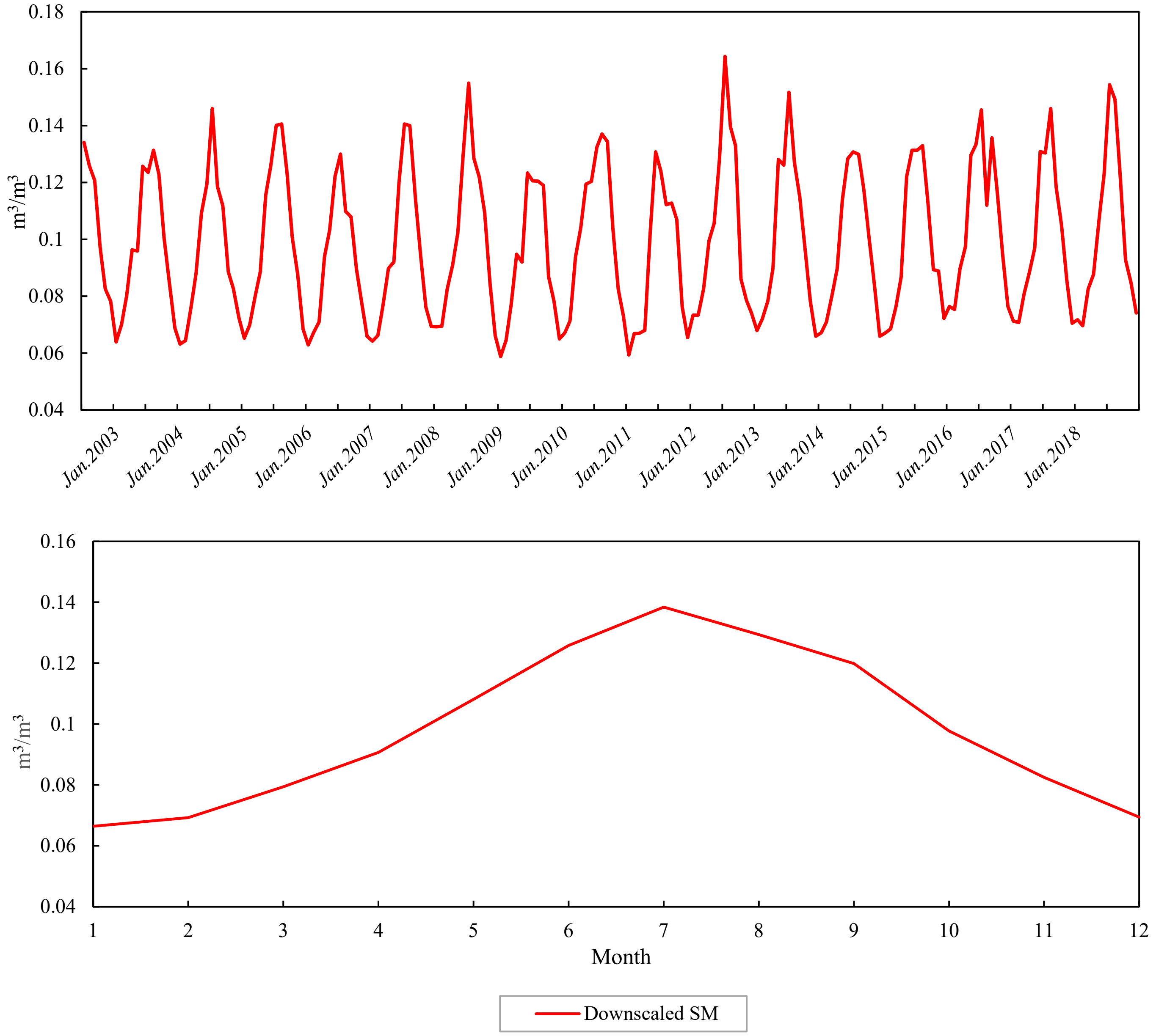

~~Figure 6: Time series of the area mean downscaled SM during the study period from June 2003 to December 2018.~~

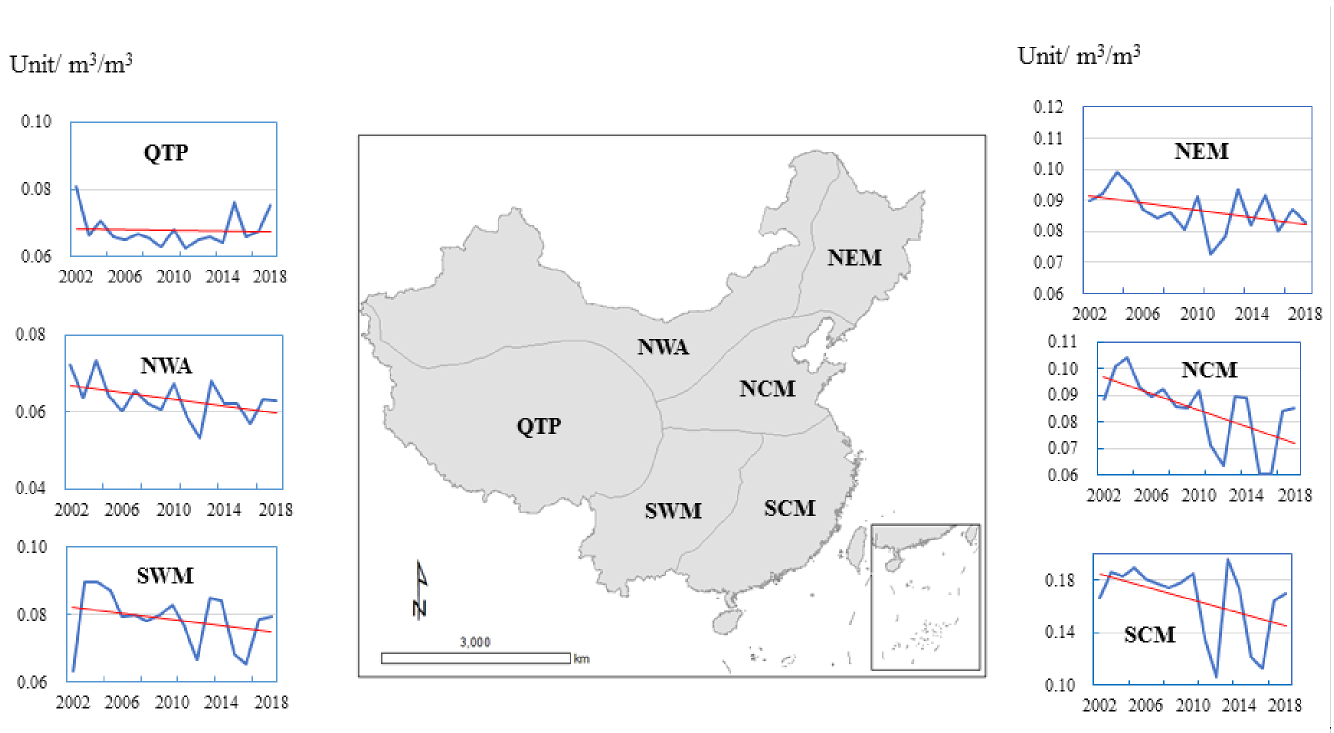

~~Figure 6: Interannual variations in the average annual SM of the six geographic regions~~

~~Note: Due to the lack of data from January to June of 2002, the annual averages are calculated from the average of only the second half; the same procedure applies to the analyses below.~~

4.2 Characteristics of the spatiotemporal variations in SM

To obtain the ~~overall~~ long-term~~ annual, seasonal and monthly~~ variations ~~of~~ in the downscaled surface SM in spatial detail, a linear regression slope is ~~was~~ conducted at the pixel level from 2002 to 2018. The slope is used to represent the variation rate of the downscaled SM. If the slope value is greater than 0, the downscaled SM ~~an increasing trend~~ becomes increasingly wet with the passage of time in the past 17 years, with a higher value indicating a more pronounced change; when the Slope value is less than 0, the surface soil water tends to become dry with the passage of time in the past 17 years, with a lower value indicating a more pronounced change; ~~and~~ a slope=0 indicates no change. Figure 7 (a) (~~left~~) is a map of the spatial trend change (slope) of SM and Figure 7 (b) is propensity slope trend values at 90% confidence level. ~~distribution map of the~~ slope. On the whole, most areas in northwestern China tend to become slightly wetter, while some parts of the eastern region become dry and some parts become slightly wetter. This result also just verified the view that people have been discussing the gradual wetness of Northwest China in recent years (Cong, et al., 2017). We think that the main reason is that global warming has promoted the intensification of the water cycle, which is the root cause of climate warming and humidification in the Northwest. For the Northwest region, water vapor mainly comes from the Arabian Sea and the Indian Ocean. As the Arctic warms, water vapor from the Arctic Ocean increases. Under the influence of air currents, the water vapor of the three places concentrated in the northwest, and the precipitation in the northwest increased rapidly, resulting in an increase in soil moisture. In the eastern monsoon region, including a small part of Inner Mongolia, the junction of Jilin and Liaoning, the North China Plain, southern Shaanxi, eastern Shanxi, and most part of Henan, Hebei and Shandong, there is a tendency to become dry, which have been reported in some studies (Liang, et al., 2017). Especially in the Huai River Basin, that is, the SCM, including Jiangsu and Zhejiang, showing a trend of drying up. In southern Guangdong, the mountainous areas of Fujian and parts of

Jiangxi show a trend of getting wet. In SWM, the Sichuan Basin is expected to become dry, and the Yunnan-Guizhou Plateau is also facing a relatively dry situation. The main reason for this phenomenon is that during this period, the southwestern region experienced high temperatures leading to a large amount of evaporation, which caused the soil moisture to decrease. This result indicates that the agricultural drought risk in SWM will increase in the future. As shown in Figure 6(b), the distribution of significant dryness changes (satisfying the 90% confidence interval) is relatively scattered, accounting for about 13% of the total pixels, mainly distributed in Horqin Sandy Land, North China Plain, Henan, Jianghuai Region, Hanjiang Plain, Dongting Lake Plain, eastern Tibet and other places. The significant wetness area is about 10% of the total pixels, mainly distributed in northwestern Qinghai and eastern Xinjiang. The main areas that become dry and wet are basically consistent with the boundary between the boundary between the first and second steps of elevation in Figure 1 and the Hu's line (the black dotted line in Figure 6). This is an interesting phenomenon, which means that precipitation and topography not only affect the spatial distribution of soil moisture, but also affect the change of SM.

~~In general, the changes in surface soil water trend from northwest to southeast, and the distribution pattern is wetter-drier. correlation coefficients, and Figure 7 (right) shows the changes in slope corresponding to the correlation coefficients. The SM changes in China have exhibited obvious geographical and seasonal differences over the past 17 years. Different slopes indicate different trends. Specifically, a slope >0 indicates an increasing trend, with a higher value indicating a more pronounced change; a slope <0 indicates a decreasing trend, with a lower value indicating a more pronounced change, and a slope=0 indicates no change. The SM changes in China have exhibited obvious geographical and seasonal differences over the past 17 years. Based on the annual SM content, the overall SM content in China has shown a slight decreasing trend, with the area of significant reduction accounting for 45.9% of the total area and the area of significant increase accounting for 49.2% of the total area. In the arid areas of the northwest, including northern Inner Mongolia and most of Xinjiang, Qinghai, and western Tibet, there is a trend of becoming wet; The trend of dry and wet changes in Qinghai and Tibet is basically the same as the trend of lake elevation changes in the region From the perspective of the different regions, in the arid areas of the northwest, there is a trend of getting wet, including northern Inner Mongolia, most of Xinjiang, and northern and western Qinghai-Tibet; among these regions, the margin of the Tarim Basin in Xinjiang has a trend of becoming dry. The conditions will become more humid, which will alleviate the current drought situation in northwestern China (Cong, et al., 2017). In the eastern monsoon region, including the junction of Inner Mongolia, Jilin and Liaoning, the North China Plain, eastern Shanxi, southern Shaanxi, and most of Henan and Hebei, except for Shandong in the coastal area, there is a drying trend. These results are in accordance with those reported Similar findings have also been reported in previous studies (Liang, et al., 2017). The monsoon area south of the Huai River, that is, the SCM including Jiangsu and Zhejiang, shows a drying trend. Regions in southern Guangdong, the mountainous areas of Fujian and parts of Jiangxi show a wetting trend. In SWM, in addition to the Sichuan Basin that tends to become dry, the Yunnan-Guizhou Plateau is also facing drier conditions. relatively obvious decreasing trends are present in the plain areas west of the Changbai Mountains in the Northeast China Monsoon Region, the Liaodong Peninsula and Shandong Peninsula in the North China Monsoon Region, the eastern coastal areas and the middle~~

~~and lower reaches of the Yangtze River Basin and the Sichuan Basin in the Southwest Wet Region, and the forest areas in the southern Qinghai-Tibet Plateau Region, and the slopes of these changes exceed 0.3 (R<-0.6).~~ This phenomenon occurred mainly because during this period, Southwest China experienced high temperatures and extensive evaporation, and these conditions contributed greatly to a regional water deficit for plants. ~~In contrast, the SM contents in the southern Hexi Corridor, the southern part of Xinjiang and the northern part of the Qinghai-Tibet Plateau in the Northwest Arid Region increased significantly, with slope values of 0.2, which is less than R>0.5. From 2002 to 2018, the SM contents in most parts of China showed a decreasing trend (except for the Northwest Arid Region), which is consistent with the analysis in Figure 6.~~ This result shows that drought risk will increase ~~throughout~~ the ~~country~~ in the SWM in the future. ~~In the Northwest Arid Region, the conditions will become more humid, which will alleviate the current drought situation in northwestern China (Cong, et al., 2017)~~. Furthermore, ~~effectively improving the ecological environment in the Northwest Arid Region of China has positive significance for western China's development and the Belt and Road Initiative.~~

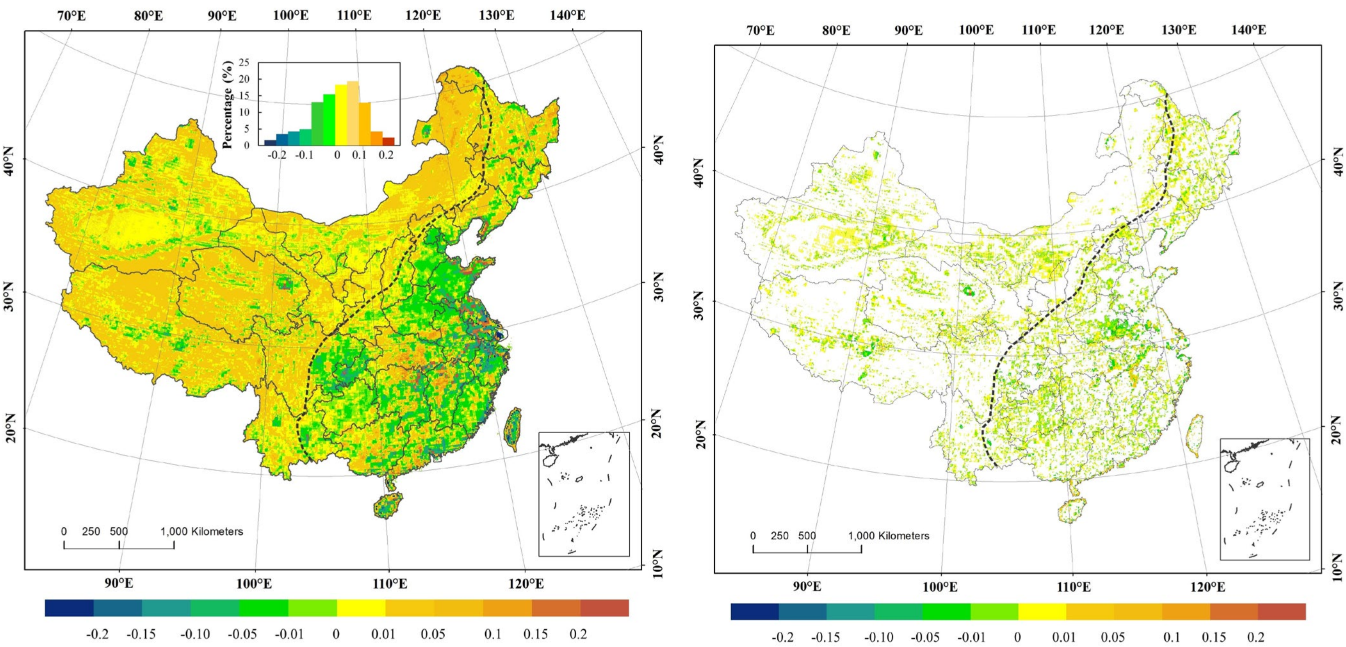

(a) (b)

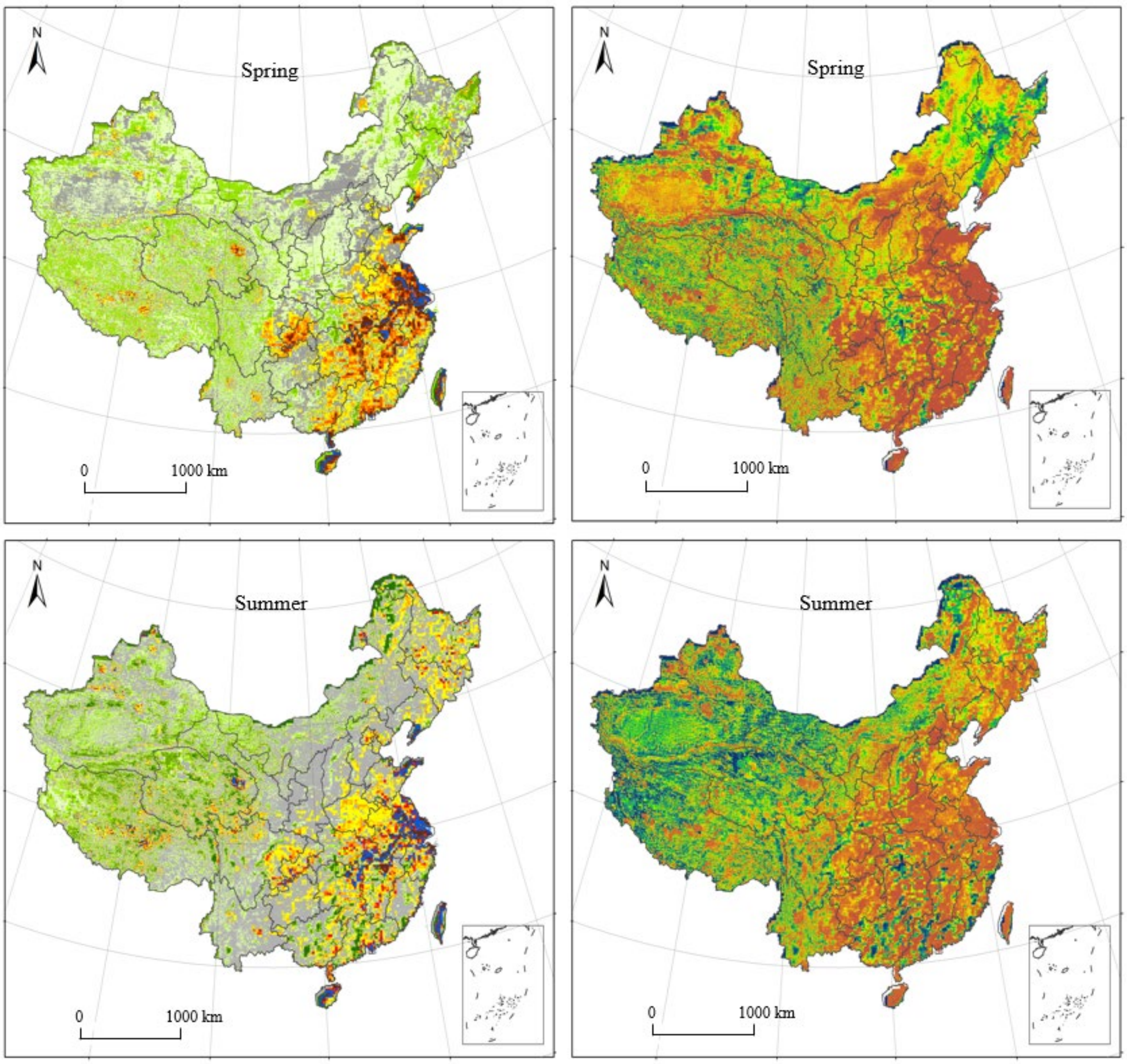
N
Spring
0
1000 km
N
Spring
0
1000 km
N
Summer
0
1000 km
N
Summer
0
1000 km

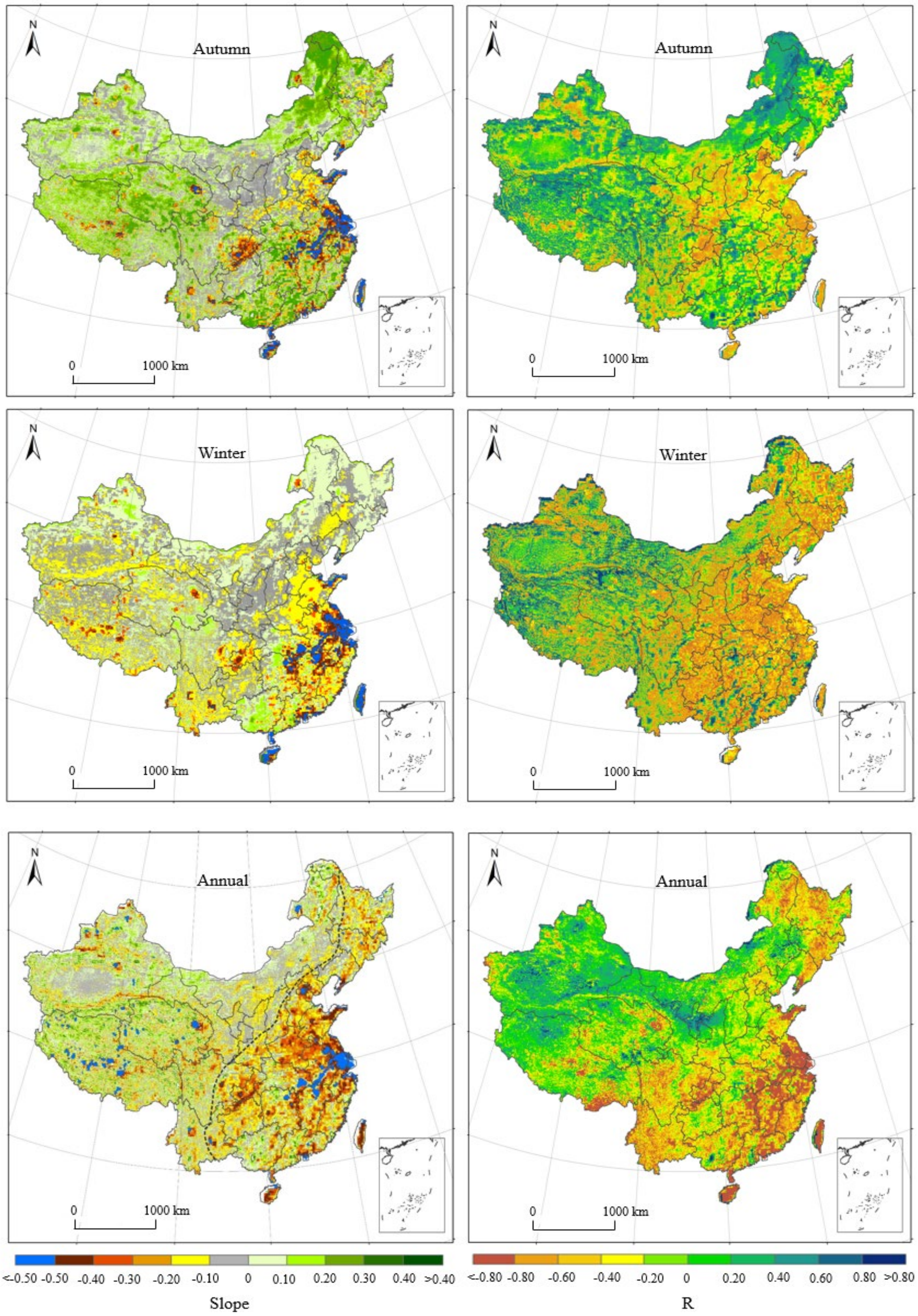

Figure 7: ~~The interannual variability rates (slope, left) and correlation coefficients (R, right) of the seasonal and annually averaged SM contents from 2002 to 2018; the dashed lines divide areas of high and low slope values.~~

Spatial distribution of annual SM variability in slope based on downscaled data from 2002 to 2018, (a) slope trend values of all pixels (b) propensity slope trend values at 90% confidence level; the black dotted line is the dividing line between wet and dry changes.

To better understand the SM changes throughout China, the spatial distributions of the annual variations in the SM for different regions in different seasons ~~were~~ are analyzed. ~~As shown in Figure 8, the overall changes in the SM throughout~~

~~China over the past 17 years exhibited obvious seasonal characteristics.~~ Figure 8 shows the pixel-level trend of SM data in each season. We found that the changes in soil moisture in spring (Figure 7 a) and autumn (Figure 7 c) are generally similar to the annual trend, while the soil moisture in most areas tends to become dry in summer (Figure 7b). Soil moisture except for a few areas in southeast China that become dry, most areas of China become wet in winter (Figure 7d).

. ~~In spring, the rate of the decrease in SM was relatively high, except in some areas of the Northeast Plain, the Three Gorges Reservoir area, and the area surrounding the Central Gobi region. More than 80% of the South China Monsoon Region showed different decreasing trends, especially in the Jiang-Huai region, and the value of the slope reached as high as -0.3 (R<-0.7). Another severe decline occurred in the Sichuan Basin during spring. In addition, in the Liaodong Peninsula, the Shandong Peninsula, and the eastern part of the Kunlun Mountains in the North China Monsoon Region, a decreasing trend predominated with a negative slope of less than -0.2 (R<-0.5). In summer, the heterogeneity of the SM among the six subregions was obvious: large change trends occurred in the northwestern Heilongjiang region of the Northwest Arid Region, the Yunnan-Guizhou Plateau in the Southwest Wet Region, and the Yangtze River plain in the South China Monsoon Region; the slope was less than -0.4 (R<-0.7). Generally, due to the large changes in the interannual hydrothermal and monsoon precipitation, the area affected by the monsoon in the east varied greatly. From spring to summer, the range of fluctuation in the SM content in the South China Monsoon Region was significantly enhanced. Usually, shifts in precipitation belts occur during the rainy season; these shifts are governed by the summer monsoon and occur during the rainy season in the Pearl River Delta and Yangtze River Delta (Zhou et al., 2010).~~ In the spring and autumn season, the line of dry and wet changes is distributed from the east to the west. The overall situation is that the east becomes drier and the west becomes wetter. The difference is that the Sichuan Basin becomes drier and the middle reaches of the Yangtze River wetter. Generally, due to the large changes in the interannual hydrothermal and monsoon precipitation, the area affected by the monsoon in the east varied greatly. From spring to summer, the range of fluctuation in the SM content in the South China Monsoon Region was significantly enhanced. Usually, shifts in precipitation belts occur during the rainy season. These shifts are governed by the summer monsoon and occur during the rainy season in the Pearl River Delta and Yangtze River Delta (Zhou et al., 2010). During the rainy season, the total rainfall was approximately 80% of the annual rainfall (Yan et al., 2015). However, in summer, there are more pixels become dry than become wet, which means of the vegetation is vulnerable to drought during the main growing season.~~. The SM contents in the Heilongjiang region in the Northeast Monsoon Region in autumn showed an extreme downward trend with a slope of less than -0.4 (R< -0.7). This trend extended to the northern part of Inner Mongolia in the Northwest Arid Region (slope<-0.4, R<-0.5), and a significant downward trend was also apparent in the hilly area of Chongqing, which is on the border between the Southwestern Wet Region and the South China Monsoon Region, with values that decreased to less than -0.3 (R < -0.5). In addition, in the Yellow-Huai River area of the North China and South China Monsoon Regions, the SM in the middle and lower reaches of the Yangtze River and the Sichuan Basin in the Southwest Wet Region showed a significant decreasing trend, and the slope in the main area decreased to less than -0.4 (R<-0.5).~~ In summer and autumn, the trends in the monsoon regions ~~were~~ are obvious. ~~Although many rainfall events occur in the summer and autumn monsoon regions, the spatial and temporal~~

~~distributions of precipitation were are not balanced. In addition, the middle and lower reaches of the Yangtze River are mainly dominated by a subtropical high-pressure system in summer, during which and a large amount of evaporation takes place, which may have been be the main cause of the observed decline decrease. The change in SM in winter was is not as significant as that those in other seasons. The decline occurred mainly in Southwest China (such as Yunnan and western Guangxi), as was also detected in previous studies (Mao, et al. 2012). The precipitation in autumn was generally low, except in the vegetation areas in the south, and there was a rising slope (slope>0.4, *R*>0.7) in the Three Gorges Dam in the upper reaches of the Yangtze River. The appearance of a decreasing slope (slope<-0.4, *R*<-0.7) is very noteworthy: it is very likely that the Three Gorges Dam will have a significant impact on the local SM variations after storage. The slopes during the four seasons in the Bohai Rim region of the North China Monsoon Region and the Yangtze River Delta region in the South China Monsoon Region were extremely high, which may have been caused by the rapid increase in the area of impervious surfaces attributable to extensive urbanization. Conversely, the SM content increased increases in areas affected by monsoons, such as the Qinghai-Tibet Plateau Region (South southern Tibet) and the Northwest Arid Region (East eastern Inner Mongolia)~~ Although many rainfall events occur in the summer and autumn monsoon regions, the spatial and temporal distributions of precipitation were not balanced. In addition, the middle and lower reaches of the Yangtze River are mainly dominated by a subtropical high-pressure system in summer, during which a large amount of evaporation takes place, which may have been the main cause of the observed decline. The change in SM in winter was not as significant as that in other seasons. Conversely, the SM content increased in areas affected by monsoons, such as the Qinghai-Tibet Plateau Region (southern Tibet) and the Northwest Arid Region (eastern Inner Mongolia).

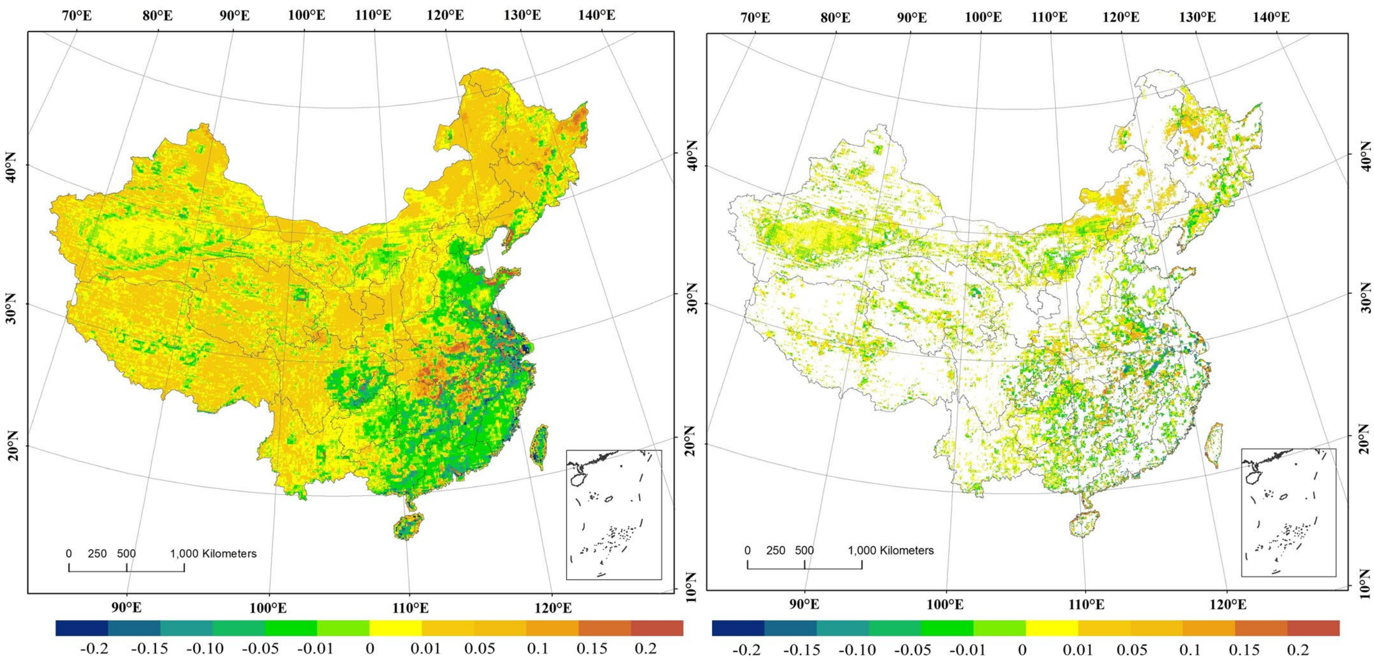

(a) (b)

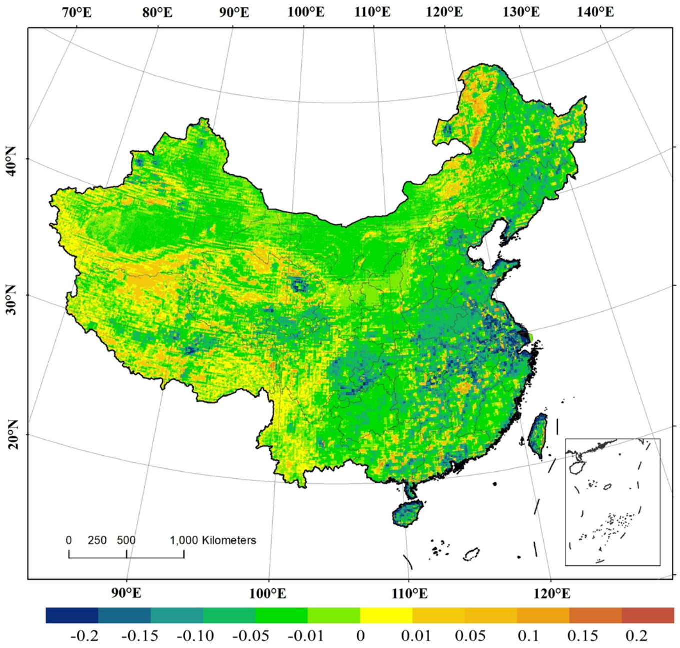
70°E 80°E 90°E 100°E 110°E 120°E 130°E 140°E
40°N 30°N 20°N 10°N
90°E 100°E 110°E 120°E
0 250 500 1,000 Kilometers
-0.2 -0.15 -0.10 -0.05 -0.01 0 0.01 0.05 0.1 0.15 0.2

(b)

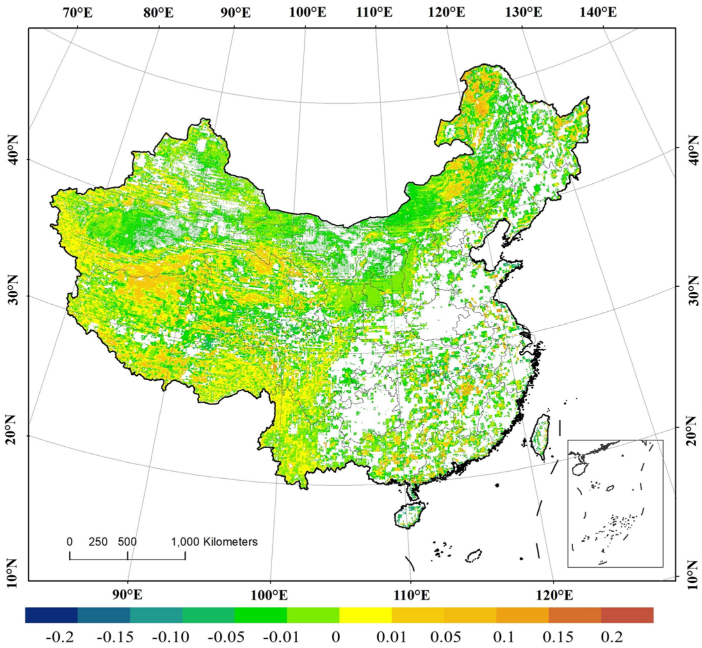
70°E 80°E 90°E 100°E 110°E 120°E 130°E 140°E
40°N 30°N 20°N 10°N
90°E 100°E 110°E 120°E
0 250 500 1,000 Kilometers
-0.2 -0.15 -0.10 -0.05 -0.01 0 0.01 0.05 0.1 0.15 0.2

(d)

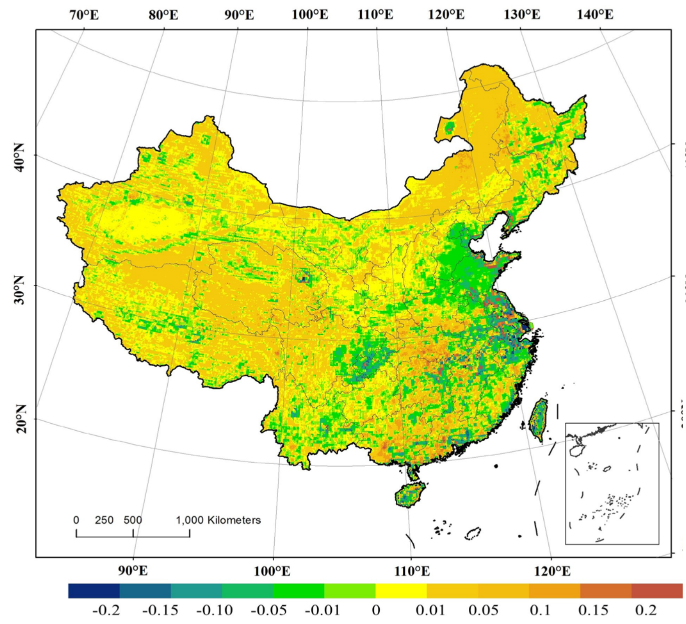
70°E 80°E 90°E 100°E 110°E 120°E 130°E 140°E
40°N 30°N 20°N
90°E 100°E 110°E 120°E
0 250 500 1,000 Kilometers
-0.2 -0.15 -0.10 -0.05 -0.01 0 0.01 0.05 0.1 0.15 0.2

(e)

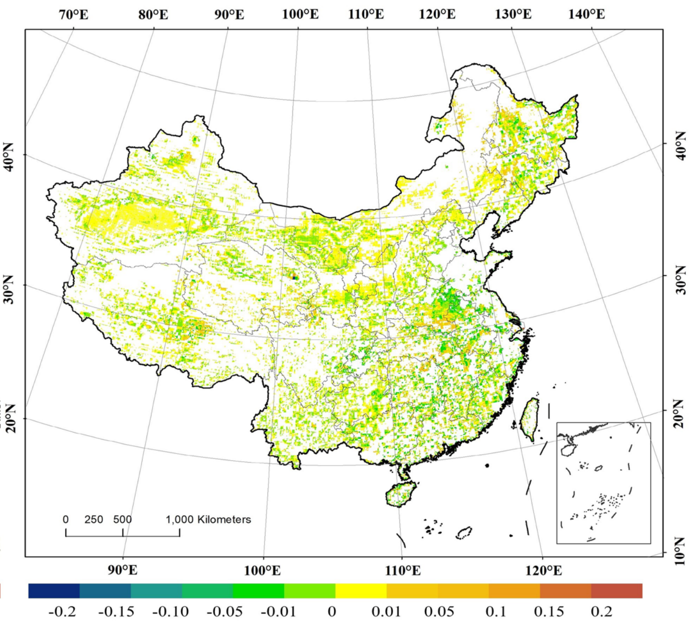
70°E 80°E 90°E 100°E 110°E 120°E 130°E 140°E
40°N 30°N 20°N 10°N
90°E 100°E 110°E 120°E
0 250 500 1,000 Kilometers
-0.2 -0.15 -0.10 -0.05 -0.01 0 0.01 0.05 0.1 0.15 0.2

(f)

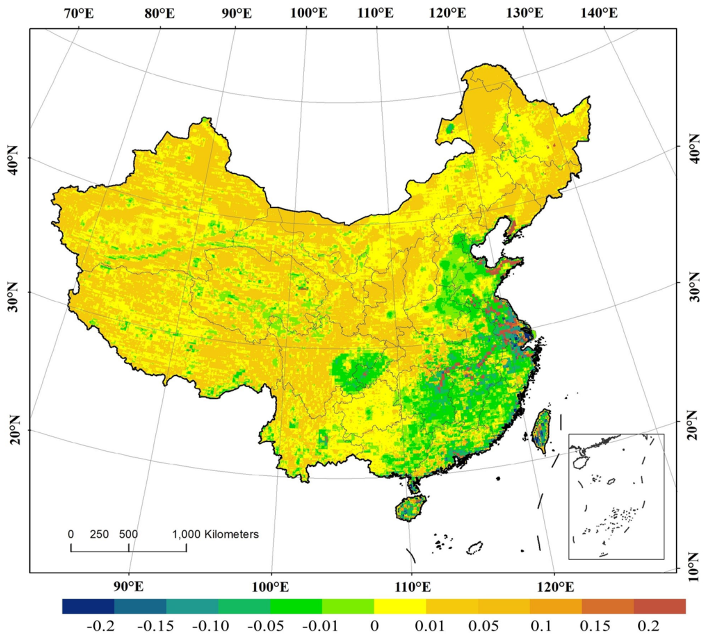
70°E 80°E 90°E 100°E 110°E 120°E 130°E 140°E
40°N 30°N 20°N 10°N
90°E 100°E 110°E 120°E
0 250 500 1,000 Kilometers
-0.2 -0.15 -0.10 -0.05 -0.01 0 0.01 0.05 0.1 0.15 0.2

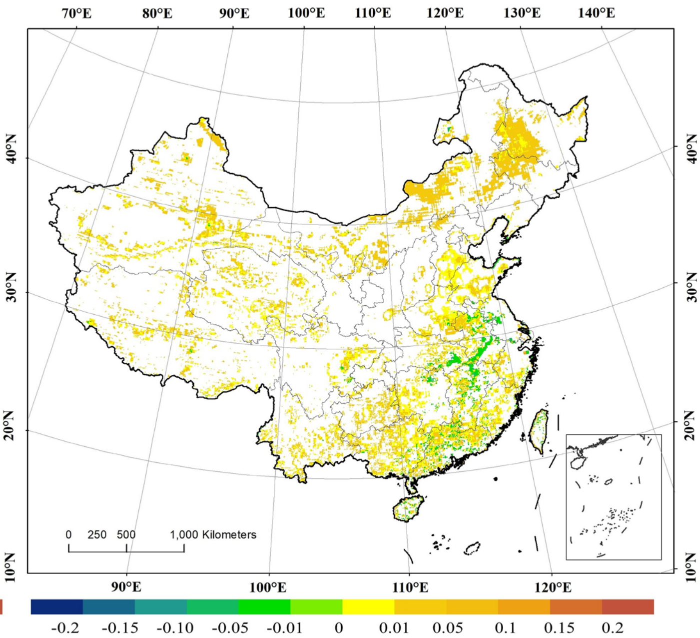
70°E 80°E 90°E 100°E 110°E 120°E 130°E 140°E
40°N 30°N 20°N 10°N
90°E 100°E 110°E 120°E
0 250 500 1,000 Kilometers
-0.2 -0.15 -0.10 -0.05 -0.01 0 0.01 0.05 0.1 0.15 0.2

(g) (h)

Figure 8 The interannual variability rates (slopes) and correlation coefficients (R) of the monthly average SM contents from 2002 to 2018.

~~We performed an analysis of the spatiotemporal changes in SM on the monthly scale in different years (Figure 8). The monthly average variability was more volatile than the variability at the seasonal and annual scales, especially in January and July. In January, northern China is under the influence of the Eurasian high-pressure center, and the monsoon in July is under the control of the subtropical Pacific high-pressure system. The South China Monsoon Region is particularly susceptible to extreme weather events (e.g., El Niño occurred in 2006 and 2015), resulting in weak summer monsoons and southerly monsoon rains in central China or south of the Yangtze River. In the northern regions, droughts and high temperatures are prone to occur in summer, and low temperatures and floods are prone to occur in the south. The low and high temperatures and heavy precipitation caused by these climatic conditions may also have been important causes of the sudden changes in SM.~~

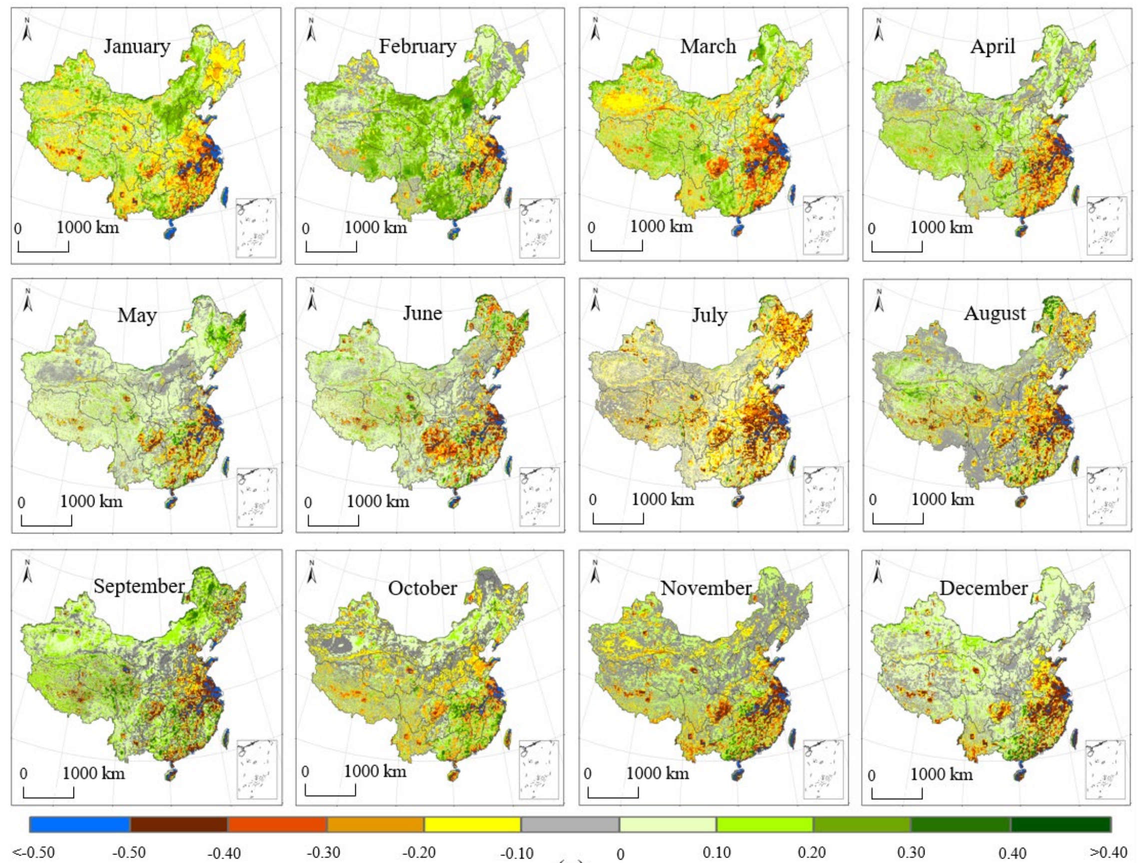

(a)

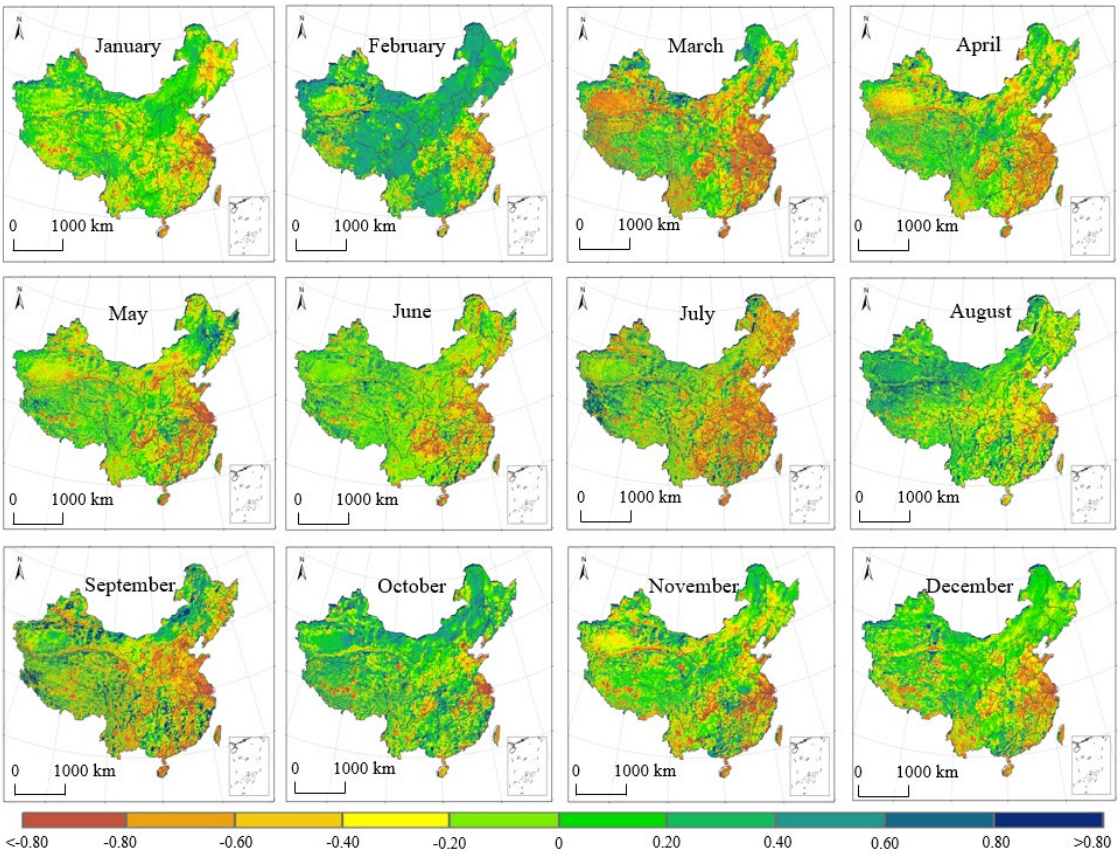

(b)

~~Figure 8: The interannual variability rates (slopes) and correlation coefficients (R) of the monthly average SM contents from 2002 to 2018. (Note: Due to the lack of data for the spring seasons of 2002 and 2018, these two phases of data are not included in the calculations.)~~

5 Data availability

The fine-resolution SSM dataset presented in this article ~~Creative Commons Attribution 4.0 International~~ is available under the Creative Commeons Attribtion 4.0 International at the following link: ~~http://doi.org/10.5281/zenodo.4049958 (Meng et al., 2020)~~ doi.org/10.5281/zenodo.4738556 (Meng et al 2021). ~~It~~ This dataset covers all of ~~China~~ China's land area at a monthly temporal resolution and a 0.05° spatial resolution from July 2002 to December 2018.

6 Discussion and conclusions

~~Global climate change has modified the spatial and temporal distributions of China's hydrologic resources, which in turn have led to changes in the Earth's biochemical cycle. SM is an important component of the Earth's biochemical cycle and not only is an important driver of the global water cycle but also potentially affects global atmospheric circulation. Access to quantitative SM information enhances not only water management, agricultural productivity, and drought monitoring capabilities but also climate prediction. Studying the high-resolution spatial and temporal characteristics of SM is of great significance for practical applications, such as water resource management, agricultural estimations, drought monitoring and climate change. Based on the 25-km spatial resolutions of the AMSR-E, SMOS, and AMSR2 microwave products, an SWD model was established using the negative correlation between the SM and TVDI for spatial data fusion to generate 0.05°-resolution long-sequence continuous SM products. The accuracy of the verified data set is satisfactory (bias: -0.024, -0.030 and -0.016 m3/m3, ubRMSE: 0.051, 0.048 and 0.042, correlation coefficient (R): 0.82, 0.88, and 0.90 on monthly, seasonal and annual scales, respectively). The data were used for a comprehensive spatial and temporal analysis of the SM status,~~

~~which revealed the characteristics and differentiation of SM in China's natural regions from 2002 to 2018. Downscaled products were used to analyze the spatial and temporal differences in SM among the six natural regions in China over the past 17 years, the results of which indicated that the SM changes in China have obvious regional and seasonal characteristics.~~

~~SM showed an overall decreasing trend, and there were some fluctuations in SM in China over the past 17 years; these fluctuations can be divided into a slow growth phase from 2002 to 2011 and a strong declining phase from 2011 to 2013. From 2014 to 2018, the SM steadily increased, and a slow decreasing phase occurred in 2010. These findings mean that SM is currently slightly decreasing, and in the next few years, China will face the risk of increased drought (especially during summer in the Southeast Monsoon Region and the North China Monsoon Region). Rapid decreasing trends occurred in the North China Monsoon Region, the South China Monsoon Region, the Yangtze River Delta region and the Bohai Sea region, while significant increasing trends occurred in the southern part of the Northwest Arid Region (in the northwestern Qinghai-Tibet Plateau). These trends can be summarized as wet in the south and dry in the north, with increases in the west and decreases in the east. In the different seasons, although the overall trends were still declining, the SM changed significantly from spring to winter. The SM was relatively evenly distributed throughout the six subregions in spring, while the SM decreased in the eastern monsoon region (the Northeast Monsoon Region, North China Monsoon Region, and South China Monsoon Region) in summer and autumn. Moreover, the inland areas (some areas in the Northwest Arid Region, the Qinghai-Tibet Plateau Region, and the Southwest Wet Region) showed an opposite trend, indicating the significant impact of summer monsoon precipitation on SM. In autumn, the SM was significantly reduced in the northeastern part of China, and grasslands dried out. Overgrazing and grassland reclamation exacerbated desert conditions. These conditions may have led to the rapid decline in SM. The monthly average change was basically the same as the seasonal average variation, but the changes were more severe. Increasing urbanization has a significant impact on SM, especially in areas with relatively rapid urbanization, such as the middle and lower reaches of the Yangtze River, the Pearl River Delta and the Bohai Rim, but not areas influenced by the monsoon. One of the factors that cannot be ignored is the decline in SM caused by the rapid expansion in the area of impervious surfaces caused by rapid urbanization.~~

Although there are many soil moisture algorithms and products, and different algorithms have their own advantages and disadvantages, and their accuracy performance is inconsistent in different regions. The main reason is that the resolution of passive microwave is too low, and the theoretical model of large-scale (mixed pixels) pixels is not very mature. Deep learning algorithms have certain advantages, but their accuracy depends on training and test data. Especially in areas with a lot of vegetation and rainfall, the accuracy performance is inconsistent for different algorithms. For example, in vegetation coverage areas, single albedo and optical thickness coefficient values are obtained differently for different retrieval algorithms, which result in some difference in soil moisture retrieval. Another difference is the treatment of heavy rainfall. When there is heavy rainfall, the retrieval error of microwave soil moisture is very large. Some retrieval algorithms determine that when there is heavy rainfall, the retrieval soil moisture is an invalid value or a null value, but some algorithms directly set the soil moisture saturation value as the soil moisture value. We need to overcome the above problems as much as possible and improve the accuracy of data products based on the observation data of SM at the site.

The global soil moisture dataset is constantly being produced, especially in recent years, the frequency of updates is getting faster and faster. Each soil moisture dataset and method of producing SM has its own advantages and disadvantages. Our SM dataset is mainly concentrated in China. Two similar sensors mounted on different satellites are used to produce a set of SM datasets that are continuous in time and space in China. For the missing part in the middle, a relatively reliable sensor was used to make up for it. In order to ensure the consistency of the time and depth of the observation data of the three instruments, we have made corrections through building reconstruction model. In particular, we took advantage of ground observation site data to make local improvements. To meet the needs of research such as agricultural drought monitoring, we downscaled the soil moisture products and obtained a higher resolution dataset.

Based on the inversion of soil moisture products using microwave sensors mounted on three different satellites, two models were established to eliminate the difference between observation time and observation depth, and a time-continuous soil moisture data set was generated for the period from 2002 to 2018. In order to further meet the needs of local monitoring and research, a downscaling model was constructed using visible light and thermal infrared data, and then the soil moisture data set was downscaled to generate a set of soil moisture data sets with spatial resolution of 0.05°. A detailed comparison and analysis with the in situ measurements shows that the reconstruction results have high precision, the bias are -0.057, −0.063 to -0.027 m3/m3, and unbiased root mean square error (ubRMSE) are 0.056, 0.036 and 0.048 m3/m3, and correlation coefficient (R) are 0.84, 0.85, and 0.89 on monthly, seasonal and annual scales, respectively). The data are freely available at http://doi.org/10.5281/zenodo.4738556 (Meng et al 2021). In order to cross-validate with the low-resolution soil moisture data set (RSSSM data, Chen et al. 2021), we upscaled the soil moisture data set and then did a cross-validation analysis. The analysis results show that the two data have a high consistency in time and space, which indirectly shows that our soil moisture data set is available. The change of soil moisture is greatly affected by rainfall, and we further analyzed the relationship between the temporal and spatial changes of soil moisture and rainfall, showing that there is a high consistency between them.

The high spatial resolution monthly SM dataset constructed for China provides a detailed perspective of the patterns of the spatial and temporal changes in SM. The SM dataset was used to analyze the regional characteristics and capture the variations in SM at the annual, seasonal and monthly scales.

The high spatial resolution monthly SM dataset constructed for China provides a detailed perspective of the patterns of the spatial and temporal changes in SM. The SM dataset was used to analyze the regional characteristics and capture the variations in SM at the annual, seasonal and monthly scales. Our results showed that the soil moisture in China has been shown generally exhibits cyclical fluctuations, which can be summarized as a slight downward trend in the southeast and a slight upward trend in the northwest. Most areas have a drying trend in summer, while most areas have the opposite in autumn. The main reason for soil moisture in Northwest China may be that global warming drives the intensification of the water cycle, which is the fundamental reason for the warming and humidification of the climate in Northwest China. For the Northwest, water vapor mainly comes from the Arabian Sea and the Indian Ocean. As the Arctic warms, water vapor from the Arctic Ocean increases. Under the action of air currents, water vapor in the three places concentrated in the northwest, and precipitation in the northwest increased rapidly, which leads to an increase in soil moisture. The dryness of southeastern China is mainly due to the increase in evaporation caused by the increase in temperature, which leads to the decrease of soil water. Of course, it may also be affected by more factors, such as El Nilo and La Niña, which requires further research in the future.

~~The increasing precipitation and artificial afforestation in the Northwest Arid Region of China have led to an increase in SM throughout this region. Surface temperatures can not only affect the evapotranspiration of SM but also indirectly affect SM by affecting influencing the transpiration of vegetation. Therefore, temperature also has a significant impact on the changes in SM. All these analyses indicate that it is very important to analyze analyzing the spatiotemporal characteristics of SM is very important for local climate change research.~~ We admit that the data set is not particularly perfectly at present. We have attempted various means to improve its applicability for users. We are working on new version, which will be friendlier to users. The availability of the data set will also be improved in the new version.

Appendix A:

1 In situ SM measured stations

The SM data provided by national agricultural gas stations (shown in Figure A1) includes relative soil humidity (%). The shallowest observation depth of the site is 10 cm to better match the surface SM. The remote sensing inversion data is expressed in volumetric water content in m3/m3. Before comparison and verification, it is necessary to perform unit conversion on the measured soil moisture site data to achieve the same amount, the formula (A1) can be used to convert the relative humidity of the site soil to the soil volumetric water content:

$$VSM = M_v * V * \rho_s \tag{A1}$$

where VSM is the soil volumetric water content (%), M_v is the relative humidity of the soil, V is the field water holding capacity, and ρ_s is the soil density.

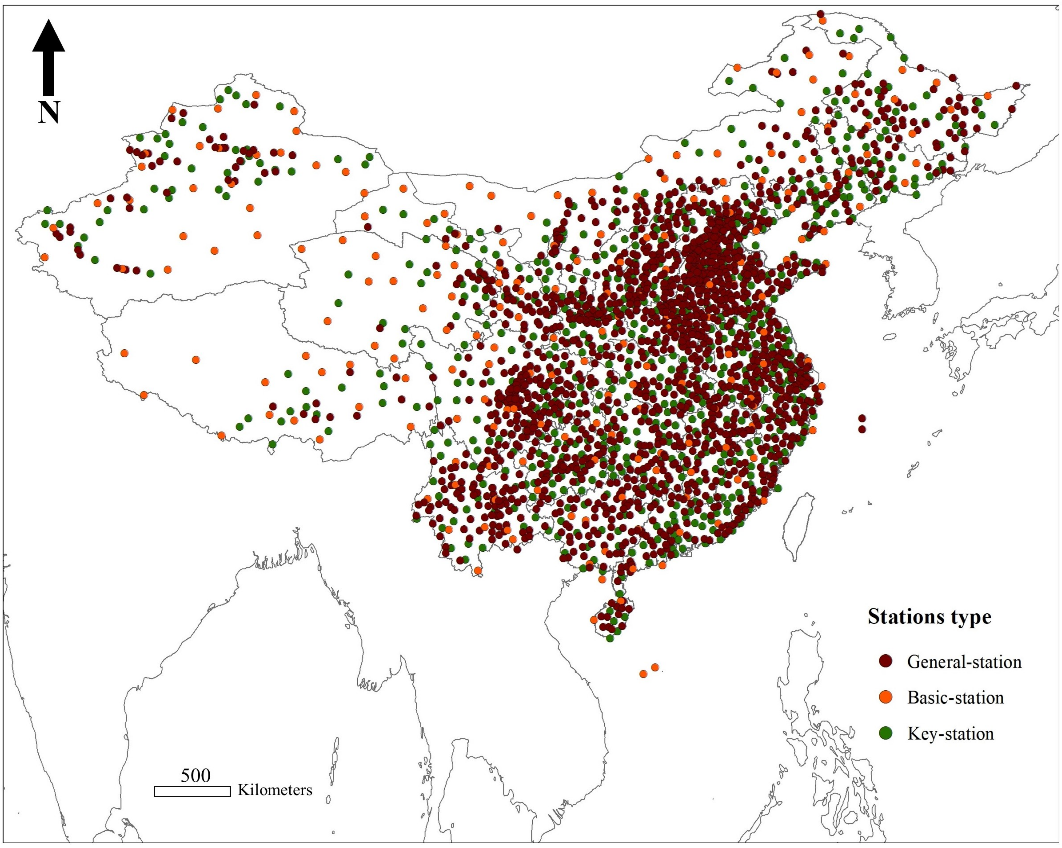

Figure A1: Distribution of agricultural meteorological stations (general station, basic station, and key station)

2 Downscaled results

Figure A2 display the original and downscaled fine resolution SM products of China, it can be seen that the downscaled SM estimates can present much more spatial details while maintaining the trend when compared with the original SM product.

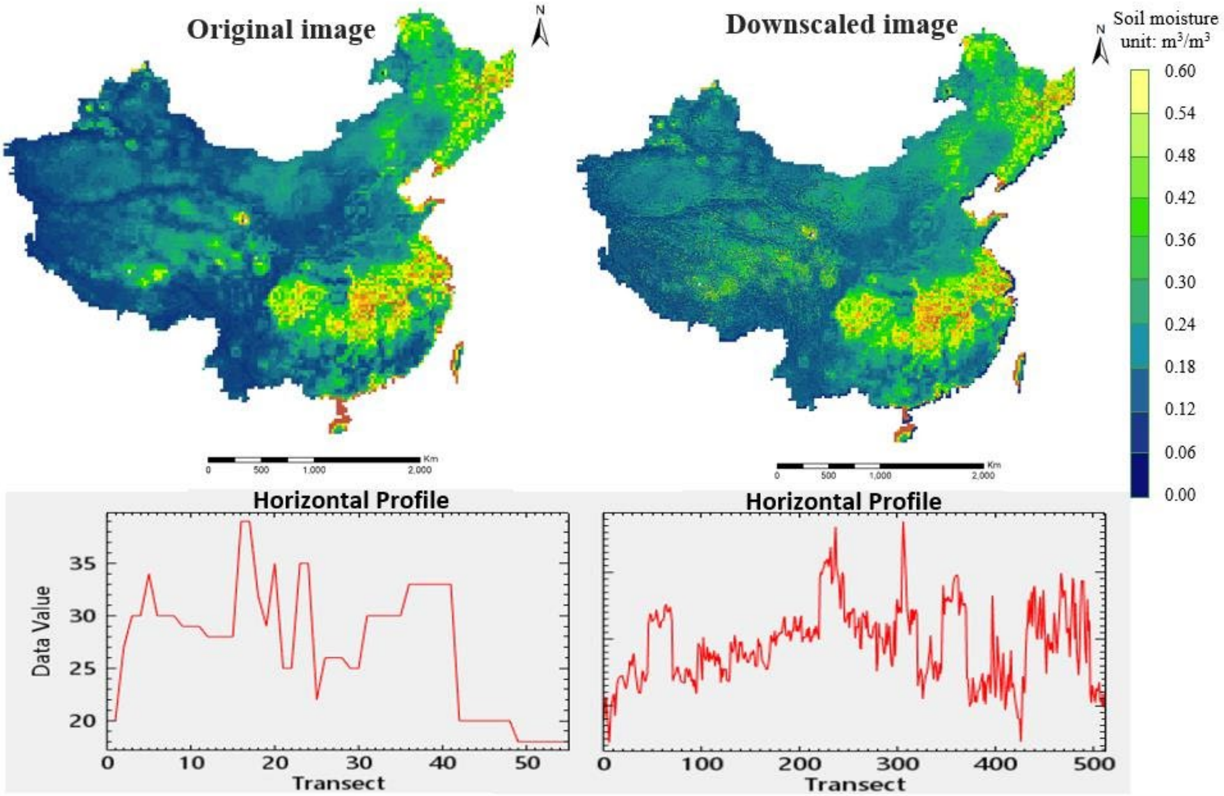

Figure A2: Comparison of downscaled SM images and original images

Appendix B:

Scatterplots of between RSSSM with downscaled SM in the six subregions are shown in Figure B1. In general, good agreements between RSSSM and downscaled SM products can be found at six subregions. It can also be observed that the overall value of downscaling products is lower compared with RSSSM, which are similar results of JAXA production reported by published studies (Zeng et al. 2015, Cui et al. 2018).

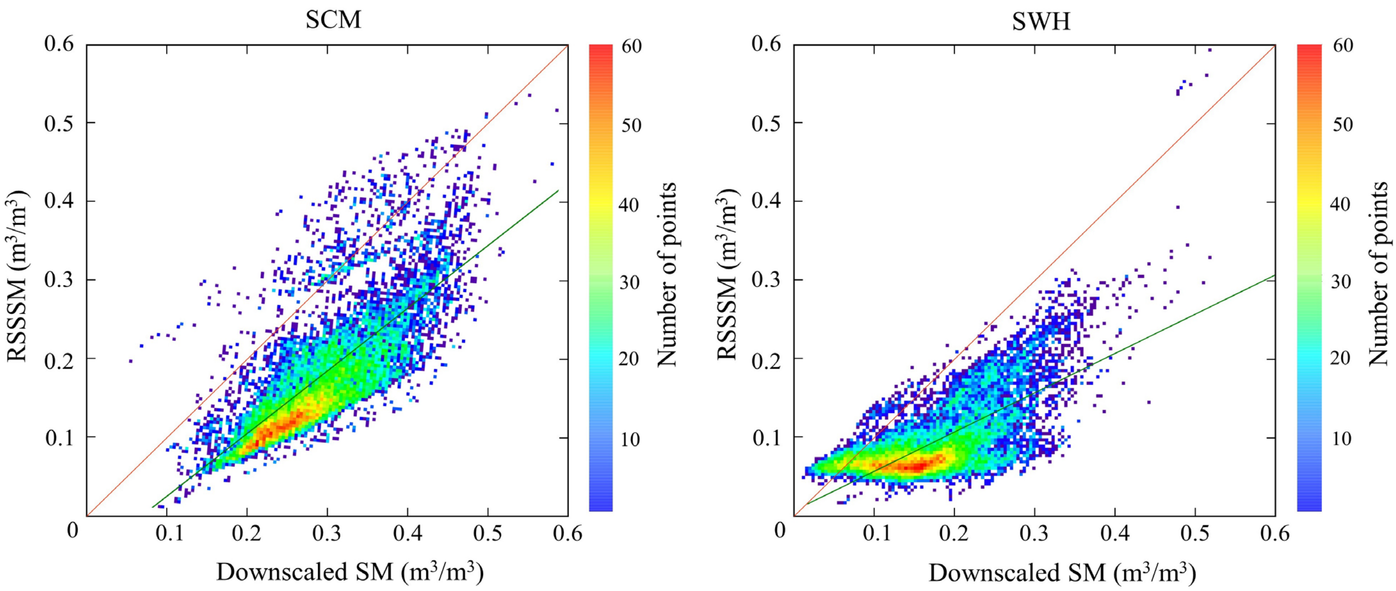

(a) (b)

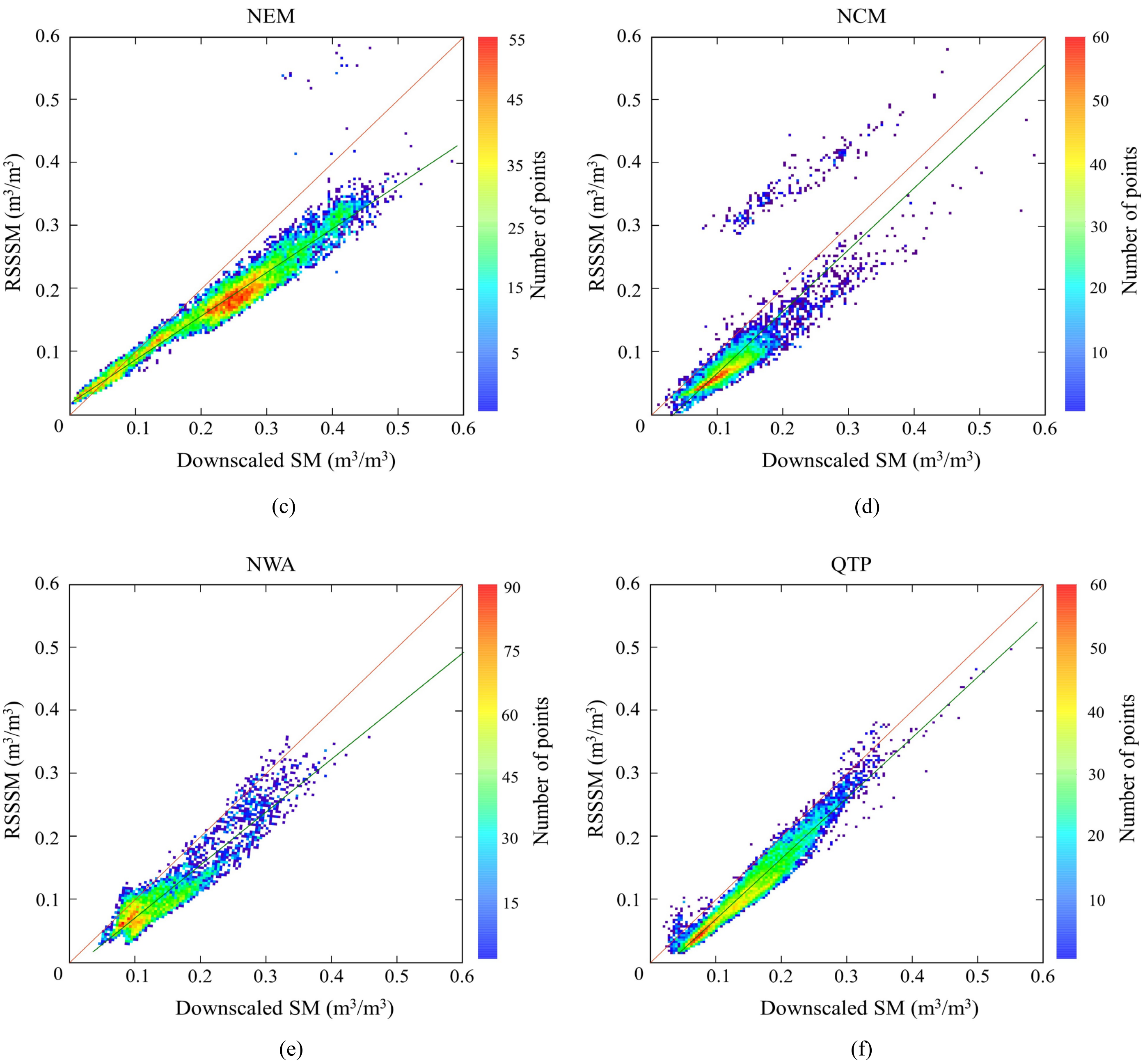

Figure B1: Scatter plot sand fitting of the RSSSM and downscaled SM dataset in six subregions

~~**Supplement.** The supplemental material related to this article is available online at: https://doi.org/10.5194/essd-10-2097-2020-supplement.~~

Author contributions. KM and FM designed the research and developed the methodology; KM and XM supervised the downloading and processing of satellite images; XM wrote the manuscript; and JS, JZ, XS, YC, LJ, ZG and all other authors revised the manuscript.

Competing interests. The authors declare that they have no conflicts of interest.

Acknowledgments. The authors thank the China Meteorological Administration for providing the ground measurements, the Japan Aerospace Exploration Agency for providing the AMSR-E and AMSR2 SM data, the ESA~~'s~~ Earth Observation User Services Portal of the European Aviation Administration for providing the SMOS-IC SM data, and the NASA~~'s~~ Earth Observing System Data and Information System for providing the MODIS LST and NDVI data and DEM data.

Financial support.

This work was supported by the National Key Project of China (Nos. 2018YFC1506602 and 2018YFC1506502), Fundamental Research Funds for Central ~~Non-profit~~ Nonprofit Scientific Institution (Grant No. 1610132020014), and the Open Fund of State Key Laboratory of Remote Sensing Science (Grant No. OFSLRSS201910).

References

Afshar, M., and Yilmaz, M.: The added utility of nonlinear methods compared to linear methods in rescaling soil moisture products, Remote Sens. Environ., 196, 224–23, https://doi.org/10.1016/j.rse.2017.05.017, 2017.

Albergel, C., DeRosnay, P., Gruhier, J. Muño, C., z-Sabater, S., Hasenauer, L., Isaksen, Y., Kerr, and Wagner. W.: Evaluation of remotely sensed and modelled soil moisture products using global ground-based in situ observations, Remote Sens. Environ., 118, 215–226, https://doi.org/10.1016/j.rse.2011.11.017, 2012.

Albergel, C., Dorigo, W., Balsamo, G., Muñoz-Sabatera, J., de Rosnay, P., Isaksen, L., and Wagner, W.: Monitoring multi-decadal satellite earth observation of soil moisture products through land surface reanalyses, Remote Sens. Environ., 138, 77-89, https://doi.org/10.1016/j.rse.2013.07.009, 2013.

Al-Yaari, A., Wigneron J. -P., Dorigo, W., Colliander, A., Pellarin, T., Hahn, S., Mialon, A., Richaume, P., Fernandez-Moran, R., Fan, L., Kerr, Y. and Lannoy, G.: Assessment and inter-comparison of recently developed/reprocessed microwave satellite soil moisture products using ISMN ground-based measurements, Remote Sens. Environ., 224, 289-303, https://doi.org/10.1016/j.rse.2019.02.008, 2019.

Bhagat, S. V.: Space-borne passive microwave remote sensing of soil moisture: a review, Recent Patents on Space Technology, 4, 119-150, https://doi.org/10.2174/221068710402150513123146#sthash.qA8fxZDt.dpuf, 2014.

Bindlish, R., Crow, W. T., and Jackson, T. J.: Role of passive microwave remote sensing in improving flood forecasts, IEEE Geosci. Remote Sens. Lett., 1, 0-116, https://doi.org/10.1109/LGRS.2008.2002754, 2009.

Brocca, L., Melone, F., Moramarco, T., Wagner, W., and Albergel, C.: Scaling and filtering approaches for the use of satellite soil moisture observations, Remote Sensing of Energy Fluxes and Soil Moisture Content, 411-426, ISBN:978-1-4665-0578-0, 2013.

Carlson, T. N., Gillies, R. R., and Perry, E. M.: A method to make use of thermal infrared temperature and NDVI measurements to infer surface soil water content and fractional vegetation cover, Remote Sens. Reviews, 9, 161–173, https://doi.org/10.1080/02757259409532220, 1994.

Cashion, J., Lakshmi, V., Bosch, D., and Jackson, T. J.: Microwave remote sensing of soil moisture: Evaluation of the TRMM microwave imager (TMI) satellite for the Little River Watershed Tifton, J. Hydr., 307, 242–253, https://doi.org/10.1016/j.jhydrol.2004.10.019, 2005.

Chauhan N. S., Miller, S., and Ardanuy, P.: Space bore soil moisture estimation at high resolution: a microwave-optical/IR synergistic approach, Int. J. Remote Sens., 24(22), 4599-4622, https://doi.org/10.1080/0143116031000156837, 2003.

Chen, C. F., Son, N. T., Chang, L. Y., and Chen, C. C.: Monitoring of soil moisture variability in relation to rice cropping systems in the Vietnamese Mekong Delta using MODIS data, Appl. Geogr., 31(2), 0-475, https://doi.org/10.1016/j.apgeog.2010.10.002, 2011.

Chen, Y., Feng, X., and Fu, B.: An improved global remote-sensing-based surface soil moisture (RSSSM) dataset covering 2003–2018, Earth Syst. Sci. Data, 13, 1–31, https://doi.org/10.5194/essd-13-1-2021, 2021.

Choi, M., and Hur, Y.: A microwave-optical/infrared disaggregation for improving spatial representation of soil moisture using AMSR-E and MODIS products, Remote Sens. Environ., 124,259–269, https://doi.org/10.1016/j.rse.2012.05.009, 2012.

Cong, D., Zhao, S., Chen, C. and Duan, Z.: Characterization of droughts during 2001-2014 based on remote sensing: a case study of Northeast China, Ecol. Inform., 39, 56–67, https://doi.org/10.1016/j.ecoinf.2017.03.005, 2017.

Crow, W. T. and Zhan, X.: Continental-scale evaluation of remotely sensed soil moisture products, IEEE Geosci. Remote Sens. Lett., 4(3), 451-455, https://doi.org/10.1109/LGRS.2007.896533, 2007.

Crow, W. T., Berg, A. A., Cosh, M. H., Loew, A., Mohanty, B. P., Panciera, R., Rosnay, P., Ryu, D., and Walker, J. P.: Upscaling sparse ground-based soil moisture observations for the validation of coarse-resolution satellite soil moisture products, Rev. Geophys., 50, RG2002,1-20, https://doi.org/10.1029/2011RG000372, 2002.

Cui, C. Y., Xu, J., Zeng, J. Y., Chen, K. S., Bai, X. J., Lu, H., Chen, Q., and Zhao, T. J., Soil moisture mapping from satellites: an intercomparison of SMAP, SMOS, FY3B, AMSR2, and ESA CCI over two dense network regions at different spatial scales. Remote Sens., 10(1), 33, https://doi.org/10.3390/rs10010033, 2018

Dorigo, W., Gruber, A., De Jeu, R., Wagner, W., Stacke, T., Loew, A., Albergel, C., Brocca, L., Chung, D., Parinussa, R., and Kidd, R.: Evaluation of the ESA CCI soil moisture product using ground-based observations, Remote Sens. Environ., 162, 380–395, https://doi.org/10.1016/j.rse.2014.07.023, 2015.

Dorigo, W., Wagner, W., Albergel, C., Albrecht, F., Balsamo, G., Brocca, L., Chung, D., Ertl, M., Forkel, M., Gruber, A., Haas, E., Hamer, D. P. Hirschi, M., Ikonen, J., De Jeu, R. Kidd, R. Lahoz, W., Liu, Y., Miralles, D., and Lecomte, P.: ESA CCI Soil Moisture for improved Earth system understanding: State-of-the art and future directions, Remote Sens. Environ., 15, 185-215, https://doi.org/10.1016/j.rse.2017.07.001, 2017.

Dorigo, W., Wagner, W., Hohensinn, R., Hahn, S., Paulik, C., Drusch, M., Mecklenburg, S., van Oevelen, P., Robck, A., and Jackson, T.: The international soil moisture network: a data hosting facility for global in situ soil moisture measurements, Hydrol. Earth Syst. Sci., 15(5), 1675–1698, https://doi.org/10.5194/hess-15-1675-2011, 2011.

Draper, C. S., Walker, J. P., and Steinle, P. J.: An evaluation of AMSR-E derived soil moisture over Australia, Remote Sens. Environ., 4, 703-710, https://doi.org/10.1016/j.rse.2008.11.011, 2009.

Fernandez-Moran, R., Al-Yaari, A. A., Mialon, A., Mahmoodi, A., Al Bitar, G., De Lannoy, N., Rodriguez-Fernandez, E., Lopez-Baeza, Y., Kerr and Wigneron, J. P.: SMOS-IC: An alternative SMOS soil moisture and vegetation optical depth product, Remote Sens., 9, 457, https://doi.org/10.3390/rs9050457, 2017.

Franz. T., Zreda, M., Rosolem, R., and Ferre, T.: A universal calibration function for determination of soil moisture with cosmic-ray neutrons. Hydrol. Earth Syst. Sci., 9(9):10303-10322, https://doi.org/10.5194/hess-17-453-2013, 2012.

González-Zamora, A., Sánchez, N., Martínez-Fernández, J., Gumuzzio, A., Piles, M., and Olmedo, E.: Long-term SMOS soil moisture products: A comprehensive evaluation across scales and methods in the Duero Basin (Spain), Phys. Chem. Earth, 83-84, 123–136, https://doi.org/10.1016/j.pce.2015.05.009, 2015.

Gruber, A., Scanlon, T., van der Schalie, R., Wagner, W., and Dorigo, W.: Evolution of the ESA CCI soil moisture climate data records and their underlying merging methodology, Earth Syst. Sci. Data, 11, 717–739, https://doi.org/10.5194/essd-11-717-2019, 2019.

Guillod, B. P., Orlowsky, B., Miralles, D. G., Teuling, A. J., and Seneviratne, S. I.: Reconciling spatial and temporal soil moisture effects on afternoon rainfall, Nat. Commun., 6, 6443, https://doi.org/10.1038/ncomms7443, 2015.

Han, E., Merwade, V., and Heathman, G. C.: Implementation of surface soil moisture data assimilation with watershed scale distributed hydrological model, J. Hydrol., 416-417, 98-117, https://doi.org/10.1016/j.jhydrol.2011.11.039, 2012.

Im, J., Park, S., Rhee, J., Baik, J., and Choi, M.: Downscaling of AMSR-E soil moisture with MODIS products using machine learning approaches, Environ. Earth Sci., 75(15), 1120,1-19, https://doi.org/10.1007/s12665-016-5917-6, 2016.

Jin, Y., Ge, Y., Wang, J., Chen, Y., Heuvelink, G. B.M., and Atkinson, P.M.: Downscaling AMSR-2 soil moisture data with Geographically weighted area-to-area regression kriging, IEEE Trans. Geosci. Remote Sensing, 56, 2362-2376, https://doi.org/10.1109/TGRS.2017.2778420, 2017.

Jing, W., Zhang, P., and Zhao, X.: Reconstructing monthly ECV global soil moisture with an improved spatial resolution, Water Resour. Manag., 32, 2523–37, https://doi.org/10.1007/s11269-018-1944-2, 2018.

Kang, C.S., Zhao, T., Shi, J., Cosh, M.H., Chen, Y., Starks, P.J., Collins, C.H., Wu, S., Sun, R., and Zheng, J.: Global soil moisture retrievals from the Chinese FY-3D microwave radiation imager. IEEE Trans. Geosci. Remote Sensing, 5, 4018 – 4032, https://doi.org/10.1109/TGRS.2020.3019408, 2020.

Kerr, Y.H., Waldteufel, P., Richaume, P., Wigneron, J.P., Ferrazzoli, P., Mahmoodi, A., Bitar, A. A., Cabot, F., Gruhier, C., Juglea, S.E., Leroux, D., Moalon, A., and Delwart, S.: The SMOS soil moisture retrieval algorithm, IEEE Trans. Geosci. Remote Sensing, 5,1384–1403, https://doi.org/10.1109/TGRS.2012.2184548, 2012.

Kim, J., and Hogue, T. S.: Improving spatial soil moisture representation through integration of AMSR-E and MODIS products, IEEE Trans. Geosci. Remote Sensing, 2, 446-460, https://doi.org/10.1109/TGRS.2011.2161318, 2012.

Kim, S., Liu, Y. Y., Johnson, F. M., Parinussa, R.M., and Sharma, A.: A global comparison of alternate AMSR2 soil moisture products: Why do they differ? Remote Sens. Environ., 61,43-62, https://doi.org/10.1016/j.rse.2015.02.002, 2015.

Koike, T., Nakamura, Y., Kaihotsu, I., Davva, G., Matsuura, N., Tamagawa, K., and Fujii, H.: Development of an advanced microwave scanning radiometer (AMSR-E) algorithm of soil moisture and vegetation water content, Proceedings of Hydr. Eng., 48, 217–222, https://doi.org/10.2208/prohe.48.217, 2004.

Lacava, T., Matgen, P., Brocca, L., Bittelli, M., Pergola, N., Moramarco, T., and Tramutoli, V.: A first assessment of the SMOS soil moisture product with in situ and modeled data in Italy and Luxembourg, IEEE Trans. Geosci. Remote Sensing, 5, 1612-1622, https://doi.org/10.1109/TGRS.2012.2186819, 2012.

Liang, L., Sun, Q., Luo, X., Wang, J., Zhang, L., Deng, M., Di, L., and Liu, Z.: Long-term spatial and temporal variations of vegetative drought based on vegetation condition index in China, Ecosphere, 8, 1-15, https://doi.org/10.1002/ecs2.1919, 2017.

Liu, L., Liao, J., Chen, X., Zhou, G., and Shao, H.: The microwave temperature vegetation drought index (MTVDI) based on AMSR-E brightness temperatures for long-term drought assessment across China (2003–2010). Remote Sens. Environ., 199, 302–320, https://doi.org/10.1016/j.rse.2017.07.012, 2017.

Liu, Y. Y., Dorigo, W. A., Parinussa, R. M., de Jeu, R.A.M., Wager, W., McCabe, M.F., Evans, J.P., and van Dijik, A.I.J.M.: Trend-preserving blending of passive and active microwave soil moisture retrievals, Remote Sens. Environ., 123, 280—297, https://doi.org/10.1016/j.rse.2012.03.014, 2012.

Liu, Y. Y., Parinussa R. M., and Dorigo, W. A.: Developing an improved soil moisture dataset by blending passive and active microwave satellite-based retrievals. Hydrol. Earth Syst. Sci., 2, 425-436, https://doi.org/10.5194/hess-15-425-2011, 2011

Liu, Y. Y., van Dijk, A. I. J. M. V., de Jeu, R., A., M., and Holmes, T., R., H.: An analysis of spatiotemporal variations of soil and vegetation moisture from a 29-year satellite-derived data set over mainland Australia, Water Resour. Res., 7, 4542-4548, https://doi.org/10.1029/2008WR007187, 2009.

Loew, A., and Schlenz, F.: A dynamic approach for evaluating coarse scale satellite soil moisture products, Hydrol. Earth Syst. Sci.,1, 75-90, https://doi.org/10.5194/hess-15-75-2011, 2011.

Loew, A., Stacke, T., Dorigo, W., Jeu, R. D., and Hagemann, S.: Potential and limitations of multidecadal satellite soil moisture observations for selected climate model evaluation studies, Hydrol. Earth Syst. Sci., 9, 3523–3542, https://doi.org/10.5194/hess-17-3523-2013, 2013.

Ma, H., Zeng J., Chen, N., Zhang, X., Cosh, M. H., and Wang,W.: Satellite surface soil moisture from SMAP, SMOS, AMSR2 and ESA CCI: A comprehensive assessment using global ground-based observations. Remote Sens. Environ., 231, 1-14, https://doi.org/10.1016/j.rse.2019.111215, 2019.

Maltese, A., Capodici, F., Ciraolo, G., and La Loggia, G.: Soil water content assessment: critical issues concerning the operational application of the triangle method, Sensors, 3, 6699-6718, https://doi.org/10.3390/s150306699, 2015.

Mao, K.B, Shi, J.C., Tang, H., Li, Z. L., Wang, X., and Chen, K. S.: A neural network technique for separating land surface emissivity and temperature from aster imagery, IEEE Trans. Geosci. Remote Sensing, 1, 200-208, https://doi.org/10.1109/TGRS.2007.907333, 2008b.

Mao, K.B., Gao, C.Y., Han, L.J., and Zhang, W.: The drought monitoring in China by using AMSR-E data, 2010 Sec. IITA Inter. Confer. on Geosci. and Remote Sens., 181–184, https://doi.org/10.1109/IITA-GRS.2010.5603008, 2010.

Mao, K.B., Ma, Y., Xia, L., Tang, H. J., and Han, L, J.: The monitoring analysis for the drought in China by using an improved MPI method, J. Integr. Agric., 6, 1048-1058, https://doi.org/10.1016/S2095-3119(12)60097-5, 2012,

Mao, K.B., Tang H. J., Zhang, L. X., Li M. C., Y., and Zhao, D. Z.: A method for retrieving soil moisture in Tibet region by utilizing microwave index from TRMM/TMI data, Int. J. Remote Sens., 29(10), 2905-2925, https://doi.org/10.1080/01431160701442104, 2008a.

Mccoll, K. A., Vogelzang, J., Konings, A.G., Entekhabi, D., Piles, María, and Stoffelen, A.: Extended triple collocation: estimating errors and correlation coefficients with respect to an unknown target, Geophys. Res. Lett., 17, 6229-6236, https://doi.org/10.1002/2014GL061322, 2014.

Meng, X., Meng, Mao, K., Meng, F., Shi, J., Zeng, J., Shen, X., Cui, Y., Liang, L., and Guo, Z.: A fine-resolution soil moisture dataset for China in 2002~2018 (Version 3.0) [Data set]. Zenodo. http://doi.org/10.5281/zenodo.4738556, 2021.

Mohanty, B., Cosh, M., Lakshmi, V., and Montzka, C.: Soil moisture remote sensing: state-of-the-science. Vadose Zone J., 1, 1-9, https://doi.org/10.2136/vzj2016.10.0105, 2017.

Molero, B., Merlin, O., Malbeteau Y, Malbéteaua, Y., Bitar, A.A., Kerr,Y., Bacon, S., Cosh, M.H., Bindlish, R., and Jackson, T.J.: SMOS disaggregated soil moisture product at 1 km resolution: Processor overview and first validation results, Remote Sens. Environ., 180, 361-376, https://doi.org/10.1016/j.rse.2016.02.045, 2016.

Moran, M. S., Clarke, T. R., Inoue, Y., and Vidal, A.: Estimating crop water deficit using the relation between surface-air temperature and spectral vegetation index. Remote Sens. Environ., 49, 246–263, https://doi.org/10.1016/0034-4257(94)90020-5, 1994.

Moran, M. S., Peters-Lidard, C. D., Watts, J. M., and Mcelroy, S.: Estimating soil moisture at the watershed scale with satellite-based radar and land surface models, Can. J. Remote Sens., 30(5), 22, https://doi.org/10.5589/m04-043, 2004.

Njoku, E. G., Jackson, T. J., Lakshmi, V., Chan, T. K., and Nghiem, S. V.: Soil moisture retrieval from AMSR-E, IEEE Trans. Geosci. Remote Sensing, 41, 215–229, https://doi.org/10.1109/TGRS.2002.808243, 2003.

Njoku, E.G., and Entekhabi, D.: Passive microwave remote sensing of soil moisture, J. Hydr., 184, 101–129, https://doi.org/10.1016/0022-1694(95)02970-2,1996.

Notaro, M.: Statistical identification of global hot spots in soil moisture feedbacks among IPCC ar4 models, J. Geophys. Res.-Atmos., 113(D9), 1-8, https://doi.org/10.1029/2007JD009199, 2008.

Owe, M., and Van de Griend, A. A.: Comparison of soil moisture penetration depths for several bare soils at two microwave frequencies and implications for remote sensing, Water Resour. Res., 34, 2319–2327, https://doi.org/10.1029/2007JD009199, 1998.

Peng, J., Loew, A., Merlin, O., and Verhoest, N. E. C.: A review of spatial downscaling of satellite remotely sensed soil moisture, Rev. Geophys., 55, 341–366, https://doi.org/10.1002/2016RG000543, 2017.

Peng, J., Loew, A., Zhang, S., Wang, J. and Niesel, J.: Spatial downscaling of satellite soil moisture data using a vegetation temperature condition index, IEEE Trans. Geosci. Remote Sensing, 54(1):558-566, https://doi.org/10.1109/TGRS.2015.2462074, 2015.

Petropoulos, G.P., Ireland, G., and Barrett, B.: Surface soil moisture retrievals from remote sensing: current status, products & future trends, Phys. Chem. Earth, A, B, C, 83,36–56, https://doi.org/10.1016/j.pce.2015.02.009, 2015.

Preimesberger, W., Scanlon, T., Su, C. -H., Gruber, A., and Dorigo, W.: Homogenization of structural breaks in the global ESA CCI soil moisture multisatellite climate data record, IEEE Trans. Geosci. Remote Sensing, 4, 2845-2862, https://doi.org/10.1109/TGRS.2020.3012896, 2021.

Rahimzadeh-Bajgiran, P., Omasa, K., and Shimizu, Y.: Comparative evaluation of the vegetation dryness index (VDI), the temperature vegetation dryness index (TVDI) and the improved TVDI (iTVDI) for water stress detection in semi-arid regions of Iran, ISPRS-J. Photogramm. Remote Sens., 68, 1-12, https://doi.org/10.1016/j.isprsjprs.2011.10.009, 2012.

Rüdiger, Christoph, Calvet, J. C., Gruhier, C., Holmes, T. R. H., De Jeu, R. A. M., and Wagner, W.: An inter comparison of ERS-scat and AMSR-E soil moisture observations with model simulations over France, J. Hydr., 2, 431-447, https://doi.org/10.1175/2008JHM997.1, 2009.

Sandholt, I., Andersen, J., and Rasmussen, K.: A simple interpretation of the surface temperature/vegetation index space for assessment of soil moisture status, Remote Sens. Environ., 2,213-224, https://doi.org/10.1016/S0034-4257(01)00274-7, 2002.

Schmugge, T., Gloersen, P., Wilheit, T., and Geiger, F.: Remote sensing of soil moisture with microwave radiometers, J. Geoph. Research, 79 (2), 317—323, 1974.

Seneviratne, S., Corti T., Davin, E., Hirschi, M., Jaeger, E., Lehner, I., Orlowsky, B., and Teuling, A.: Investigating soil moisture-climate interactions in a changing climate: A review, Earth-Sci. Rev., 99(3-4):125-161, https://doi.org/10.1016/j.earscirev.2010.02.004, 2010.

Shen, X., Mao, K., Q. Qin, Y., and Zhang, G.: Bare surface soil moisture estimation using double-angle and dual-polarization L-band radar data, IEEE Trans. Geosci. Remote Sensing, 51(7), 3931-3942, https://doi.org/10.1109/TGRS.2012.2228209, 2013.

Shi, J., Du, Y., Du, J. Y., Jiang, L. M., Chai, L. N., Mao, K. B., Xu, P., Ni, W., J., Xiong, C., Liu, Q., Liu, C.Z., Guo, P., Cui, Q., Li, Y.,Q., Chen, J., Wang, A., Q., Luo, H., J., and Wang., Y., H.: Progresses on microwave remote sensing of land surface parameters, Sci. China-Earth Sci., 7, 1052-1078, https://doi.org/10.1007/s11430-012-4444-x, 2012.

Shi, J., Jiang, L., Zhang, L., Chen, K., Wigneron, J., Chanzy, A., and Jackson, T.: Physically based estimation of bare-surface soil moisture with the passive radiometers, IEEE Trans. Geosci. Remote Sensing, 44(11), 3145-3153, https://doi.org/10.1109/TGRS.2006.876706, 2006.

Srivastava, P., Pandey, V., Suman, S., Gupta, M., and Islam, T.: Chapter 2 - Available Data Sets and Satellites for Terrestrial Soil Moisture Estimation, Satellite Soil Moisture

Retrieval, 29–44, 2016.

Srivastava, P.: Satellite soil moisture: review of theory and applications in water resources, Water Resour. Manag., 31(10), 3161-3176, https://doi.org/10.1007/s11269-017-1722-6, 2017.

Su, Z., Dorigo, W., Fernández-Prieto, D., Van Helvoirt, M., Hungershoefer, K., de Jeu, R., Parinussa, R., Timmermans, J., Roebeling, R., Schroder, M., Schulz, J., Van der Tol, C., Stammes, P., Wagner, W., Wang, L., Wang, P., and Wolters, E.: Earth observation water cycle multi-mission observation strategy (WACMOS), Hydrology Earth System Sciences Discussions, 7, 7899–7956, https://doi.org/10.5194/hessd-7-7899-2010, 2010.

Taylor, C. M., Gounou, A., Guichard, F., Harris, P. P., Ellis, R. J., Couvreux, F., and Kauwe, M.: Frequency of Sahelian storm initiation enhanced over mesoscale soil-moisture patterns, Nat. Geosci., 7, 430-433, https://doi.org/10.1038/ngeo1173, 2011.

Wang, J., Ling. Z., Yang, W., and Zeng, H.: Improving spatial representation of soil moisture by integration of microwave observations and the temperature–vegetation–drought index derived from MODIS products, ISPRS-J. Photogramm. Remote Sens., 113,144-154, https://doi.org/10.1016/j.isprsjprs.2016.01.009, 2016.

Yan, J., Li, K., Wang, W., Zhang, D., and Zhou, G.: Changes in dissolved organic carbon and total dissolved nitrogen fluxes across subtropical forest ecosystems at different successional stages, Water Resour. Res., 51 (5), 3681–3694, https://doi.org/10.1002/2015WR016912, 2015.

Yan, Y. B., Mao, K. B., Shi, J., Piao, S. L., Shen, X. Y., Dozier, J., Liu, Y., Ren, H. L, and Bao, Q.: Driving forces of land surface temperature anomalous changes in North America in 2002–2018, Sci. Rep., 6931(10), 1-13, https://doi.org/10.1038/s41598-020-63701-5, 2020.

Yilmaz, M. T., and Crow, W. T.: The optimality of potential rescaling approaches in land data assimilation. J. Hydr., 14(2):650-660, https://doi.org/10.1175/JHM-D-12-052.1, 2013.

Zeng, J., Chen, K. S., Cui, C., and Bai, X.: A physically based soil moisture index from passive microwave brightness temperatures for soil moisture variation monitoring, IEEE Trans. Geosci. Remote Sensing, 58(4), 2782-2795, https://doi.org/10.1109/TGRS.2019.2955542, 2020.

Zeng, J., Li, Z., Chen, Q., Bi, H., Qiu, J., and Zou, P.: Evaluation of remotely sensed and reanalysis soil moisture products over the Tibetan Plateau using in-situ observations, Remote Sens. Environ., 163, 91–110, https://doi.org/10.1016/j.rse.2015.03.008, 2015.

Zhao, B., Mao, K. B., Cai, Y., Shi, J., Li, Z., Qin, Z., and Meng, X.: A combined Terra and Aqua MODIS land surface temperature and meteorological station data product for China from 2003 – 2017, Earth Syst. Sci. Data, 12, 2555–2577, https://doi.org/10.5194/essd-12-2555-2020, 2020.

Zhao, J., and Chen, C. K.: China's geography, Higher Education Press, Beijing, China, 2011.

Zhao, S., Cong, D., He, K., Yang, H., and Qin, Z.: Spatial-temporal variation of drought in china from 1982 to 2010 based on a modified temperature vegetation drought index (mTVDI), Sci. Rep., 7(1), 17473, https://doi.org/10.1038/s41598-017-17810-3, 2017.

Zhao, W., Sánchez, N., Lu, H., and Li, A.: A spatial downscaling approach for the SMAP passive surface soil moisture product using random forest regression, J. Hydr., 563, 1009-1024, https://doi.org/10.1016/j.jhydrol.2018.06.081, 2018.

Zhou, G., Wei, X., Luo, Y., Zhang, M., and Wang, C.: Forest recovery and river discharge at the regional scale of Guangdong province, Water Resour. Res., 9, 5109-5115, https://doi.org/10.1029/2009WR008829, 2010.

Zwieback, S., Su, C.H., Gruber, A., Dorigo, W.A., and Wagner, W.: The impact of quadratic nonlinear relations between soil moisture products on uncertainty estimates from triple collocation analysis and two quadratic extensions, J. Hydr., 17, 1725-1743, https://doi.org/10.1175/JHM-D-15-0213.1, 2016.